



Publication Year	2018
Acceptance in OA	2020-11-02T13:40:04Z
Title	LBT/MODS spectroscopy of globular clusters in the irregular galaxy NGC 4449
Authors	ANNIBALI, FRANCESCA, Morandi, E., Watkins, L. L., TOSI, Monica, Aloisi, A., BUZZONI, Alberto, CUSANO, FELICE, FUMANA, Marco, Marchetti, A., MIGNOLI, Marco, Mucciarelli, A., ROMANO, Donatella, van der Marel, R. P.
Publisher's version (DOI)	10.1093/mnras/sty344
Handle	http://hdl.handle.net/20.500.12386/28113
Journal	MONTHLY NOTICES OF THE ROYAL ASTRONOMICAL SOCIETY
Volume	476

LBT/MODS spectroscopy of globular clusters in the irregular galaxy NGC 4449

F. Annibali,^{1★} E. Morandi,² L. L. Watkins,^{3★} M. Tosi,^{1★} A. Aloisi,³ A. Buzzoni,¹
F. Cusano,¹ M. Fumana,⁴ A. Marchetti,⁴ M. Mignoli,¹ A. Mucciarelli,^{1,2} D. Romano¹
and R. P. van der Marel³

¹INAF–Osservatorio di Astrofisica e Scienza dello Spazio di Bologna, Via Piero Gobetti, 93/3, I-40129 Bologna, Italy

²Dipartimento di Fisica e Astronomia, Università di Bologna, via Piero Gobetti 93/2, I-40129 Bologna, Italy

³Space Telescope Science Institute, 3700 San Martin Drive, Baltimore, MD 21218, USA

⁴INAF–Istituto di Astrofisica Spaziale e Fisica Cosmica, Via Bassini 15, I-20133 Milano, Italy

Accepted 2018 February 6. Received 2018 February 6; in original form 2017 December 22

ABSTRACT

We present intermediate-resolution ($R \sim 1000$) spectra in the ~ 3500 – $10\,000$ Å range of 14 globular clusters in the Magellanic irregular galaxy NGC 4449 acquired with the Multi-Object Double Spectrograph on the Large Binocular Telescope. We derived Lick indices in the optical and the Ca II triplet index in the near-infrared in order to infer the clusters' stellar population properties. The inferred cluster ages are typically older than ~ 9 Gyr, although ages are derived with large uncertainties. The clusters exhibit intermediate metallicities, in the range $-1.2 \lesssim [\text{Fe}/\text{H}] \lesssim -0.7$, and typically sub-solar $[\alpha/\text{Fe}]$ ratios, with a peak at ~ -0.4 . These properties suggest that (i) during the first few Gyr NGC 4449 formed stars slowly and inefficiently, with galactic winds having possibly contributed to the expulsion of the α -elements, and (ii) globular clusters in NGC 4449 formed relatively 'late', from a medium already enriched in the products of Type Ia supernovae. The majority of clusters appear also underabundant in CN compared to Milky Way halo globular clusters, perhaps because of the lack of a conspicuous N-enriched, second generation of stars like that observed in Galactic globular clusters. Using the cluster velocities, we infer the dynamical mass of NGC 4449 inside 2.88 kpc to be $M(<2.88 \text{ kpc}) = 3.15_{-0.75}^{+3.16} \times 10^9 M_{\odot}$. We also report the serendipitous discovery of a planetary nebula within one of the targeted clusters, a rather rare event.

Key words: galaxies: abundances – galaxies: dwarf – galaxies: individual: NGC 4449 – galaxies: irregular – galaxies: starburst – galaxies: star clusters: general.

1 INTRODUCTION

Dwarf galaxies are extremely important for our understanding of cosmology and galaxy evolution for several reasons: (i) they are the most frequent type of galaxy in the Universe (e.g. Lilly et al. 1995); (ii) in the Λ cold dark matter cosmological scenario, they are considered to be the first systems to collapse, supplying the building blocks for the formation of more massive galaxies through merging and accretion (e.g. Kauffmann & White 1993); (iii) dwarf galaxies that experienced star formation (SF) at redshift $z > 6$ are believed to be responsible for the reionization of the Universe (e.g. Bouwens et al. 2012); (iv) due to their low potential well, dwarf galaxies are highly susceptible to loss of gas and metals (either because of galactic outflows powered by supernova (SN) explosions or because of

environmental processes) and thus provide an important contribution to the enrichment of the intergalactic medium. Deriving how and when dwarf galaxies formed their stars is therefore fundamental to studies of galaxy formation and evolution.

The most straightforward and powerful way to derive a galaxy's star formation history (SFH) is by resolving its stellar content: high signal-to-noise photometry of individual stars directly translates into deep colour–magnitude diagrams (CMDs) that can be modelled to reconstruct the behaviour of the star formation rate (SFR) as a function of look-back time (e.g. Tosi et al. 1991; Bertelli et al. 1992; Gallart et al. 1996; Dolphin 1997; Grocholski et al. 2012; Cignoni et al. 2016). Indeed, since the advent of the *Hubble Space Telescope* (HST), the study of resolved stellar populations in a large number of galaxies within the Local Group and beyond has received a tremendous boost (e.g. Annibali et al. 2009, 2013; Dalcanton et al. 2009; McQuinn et al. 2010a; Weisz et al. 2014; Sacchi et al. 2016). However, the look-back time that can be reached critically depends on the depth of the CMD: accurate information on the

* E-mail: francesca.annibali@oabo.inaf.it (FA); lwatkins@stsci.edu (LLW); monica.tosi@oabo.inaf.it (MT)

earliest epochs is only possible by reaching the oldest, faintest main-sequence turnoffs and this translates, even with the superb spatial resolution of *HST*, into a typical distance of $\lesssim 1$ Mpc from us. This distance limit corresponds in practice to a limit on the galaxy types for which the most ancient SFH can be accurately recovered, the large majority of systems included in this volume being dwarf spheroidals (dSphs). With the obvious exception of the Magellanic Clouds, late-type, star-forming dwarfs are found at larger distances than dSphs, and the most active nearby star-forming dwarfs (e.g. NGC 1569, NGC 1705, NGC 4449) are as far as $D \gtrsim 3$ Mpc.

Spectroscopic studies of (unresolved) star clusters provide an alternative approach to gather insights into the past SFH. Such studies are particularly valuable in those cases where the resolved CMD does not reach much below the tip of the red-giant branch (RGB), making it impossible to resolve the details of the SFH prior to 1–2 Gyr ago. Indeed, star clusters are present in all types of galaxies and are suggested to be the birth site of many (possibly most) stars. The formation of massive star clusters is thought to be favoured by the occurrence of intense SF events, as suggested by the presence of a correlation between the cluster formation efficiency and the galaxy SFR density (e.g. Larsen & Richtler 2000; Goddard, Bastian & Kennicutt 2010; Adamo et al. 2011a, 2015). Therefore, clusters can be powerful tracers of the SF process in their host galaxies.

Despite the large number of photometric studies of clusters in dwarf galaxies performed so far (e.g. Hunter et al. 2000; Hunter 2001; Billett, Hunter & Elmegreen 2002; Annibali et al. 2009, 2011b; Adamo, Östlin & Zackrisson 2011b; Cook et al. 2012; Pellerin et al. 2012), only a few systems (early-type dwarfs, in the majority of cases) have been targeted with 6–10 m class telescopes to derive cluster spectroscopic ages and chemical composition (e.g. Puzia et al. 2000; Strader, Brodie & Huchra 2003; Strader et al. 2005; Conselice 2006; Sharina, Puzia & Krylatyh 2007; Sharina et al. 2010; Strader, Seth & Caldwell 2012). Although spectroscopic ages older than ~ 2 Gyr are derived with large uncertainties, both because of the well-known age–metallicity degeneracy and because of the progressively lower age sensitivity of the Balmer absorption lines with increasing look-back time, the additional information on the chemical abundance ratios can provide stringent constraints on the galaxy SFH back to the earliest epochs.

In this paper, we present deep spectroscopy obtained with the Large Binocular Telescope (LBT) of clusters in the Magellanic irregular galaxy NGC 4449 ($\alpha_{2000} = 12^{\text{h}}28^{\text{m}}11^{\text{s}}.9$ $\delta_{2000} = +44^{\circ}05'40''$) at a distance of 3.82 ± 0.18 Mpc from us (Annibali et al. 2008). With an integrated absolute magnitude of $M_B = -18.2$, NGC 4449 is ≈ 1.4 times more luminous than the Large Magellanic Cloud (LMC). Its metallicity has been derived through spectroscopy of H II regions and planetary nebulae (PNe; e.g. Berg et al. 2012; Pilyugin, Grebel & Zinchenko 2015; Annibali et al. 2017), and ranges between $12 + \log(\text{O}/\text{H}) = 8.26 \pm 0.09$ and 8.37 ± 0.05 , close to the LMC value, although Kumari, James & Irwin (2017) found a metallicity as low as $12 + \log(\text{O}/\text{H}) = 7.88 \pm 0.14$ in the very central galaxy regions. NGC 4449 is remarkable for several reasons: it is one of the most luminous and active nearby irregular galaxies, with a current SFR of $\sim 1 M_{\odot} \text{ yr}^{-1}$ (McQuinn et al. 2010b; Sacchi et al. 2018); it has a conspicuous population of clusters (≈ 80), with a specific frequency of massive clusters higher than in nearby spirals and in the LMC (Annibali et al. 2011b); it hosts an old, very massive, and elliptical cluster, associated with two tails of young stars, that has been suggested to be the nucleus of a former gas-rich satellite galaxy undergoing tidal disruption by

NGC 4449 (Annibali et al. 2012); it is the first dwarf galaxy where a stellar tidal stream has been discovered (Martínez-Delgado et al. 2012; Rich et al. 2012); it has a very extended H I halo (~ 90 kpc in diameter) that is a factor of ~ 10 larger than the optical diameter of the galaxy, and that appears to rotate in the opposite direction to the gas in the centre (Hunter et al. 1998). All these studies suggest that NGC 4449 experienced a complex evolution and was possibly built, at least in part, through the accretion of satellite galaxies.

From optical CMDs of the stars resolved with the Advanced Camera for Survey (ACS) onboard *HST*, McQuinn et al. (2010b) and Sacchi et al. (2018) derived the SFH of NGC 4449. These analyses indicate that NGC 4449 enhanced its SF activity ~ 500 Myr ago, while the rate was much lower at earlier epochs; however, the impossibility of reaching the old main-sequence turnoffs or even the red clump/horizontal branch with the available data implies that the SFH of NGC 4449 is very uncertain prior to ~ 1 – 2 Gyr ago. Star clusters appear mostly unresolved in NGC 4449; Annibali et al. (2011b) performed integrated-light photometry of ~ 80 young and old clusters identified in the ACS images, and found that their colours are compatible, under the assumption of a metallicity of $\sim 1/4$ solar, with a continuous age distribution over the whole Hubble time. However, only spectroscopy can allow for real progress by breaking, to some extent, the age–metallicity degeneracy and by providing information on the element abundance ratios. Motivated by this goal, we performed a spectroscopic follow-up of a few clusters in the Annibali et al. (2011b) sample using the Multi-Object Double Spectrographs (MODS) on the LBT. In Section 2, we describe the observations and the data reduction; in Section 3, we compute optical and near-infrared absorption-line indices; in Section 4, we derive the cluster stellar population parameters; in Section 5, we present our serendipitous discovery of a candidate PN within one of the clusters; in Section 6, we obtain an estimate of the dynamical mass of NGC 4449 from cluster velocities; in Sections 7 and 8, we discuss and summarize our results.

2 OBSERVATIONS AND DATA REDUCTION

Clusters to be targeted for spectroscopy were selected from the catalogue of Annibali et al. (2011b), hereafter *A11*, based on the *HST*/ACS *F435W* (*B*), *F555W* (*V*), and *F814W* (*I*) images acquired within GO programme 10585, PI: Aloisi. We selected 14 clusters located in relatively external regions of NGC 4449 to avoid the severe crowding towards the most central star-forming regions. The observations were performed with the MODS instrument on the LBT in 2013 January 21 and 22 within programme 2012B_23, run B (PI: Annibali). The $1 \text{ arcsec} \times 8 \text{ arcsec}$ slit mask superimposed on the ACS *V* image is shown in Fig. 1, while Fig. 2 shows colour-composite ACS images for the target clusters. The observations were obtained with the blue G400L (3200–5800 Å) and the red G670L (5000–10 000 Å) gratings on the blue and red channels in dichroic mode for 8×1800 s, for a total integration time of 4 h. Notice that the instrumental sensitivity in dichroic mode is very low in the ~ 5500 – 5800 Å range. The seeing varied from ~ 0.7 to ~ 0.9 arcsec, and the average airmass was ~ 1.4 . The journal of the observations is provided in Table 1. Three Lick standard stars of F–K spectral types (see Table 2) were also observed during our run with a $1 \text{ arcsec} \times 8 \text{ arcsec}$ long slit with the purpose of calibrating our measurements into the widely used Lick–IDS system (see Section 3 for more details).

Bias and flat-field subtraction, and wavelength calibrations were performed with the Italian LBT Spectroscopic Reduction Facility at

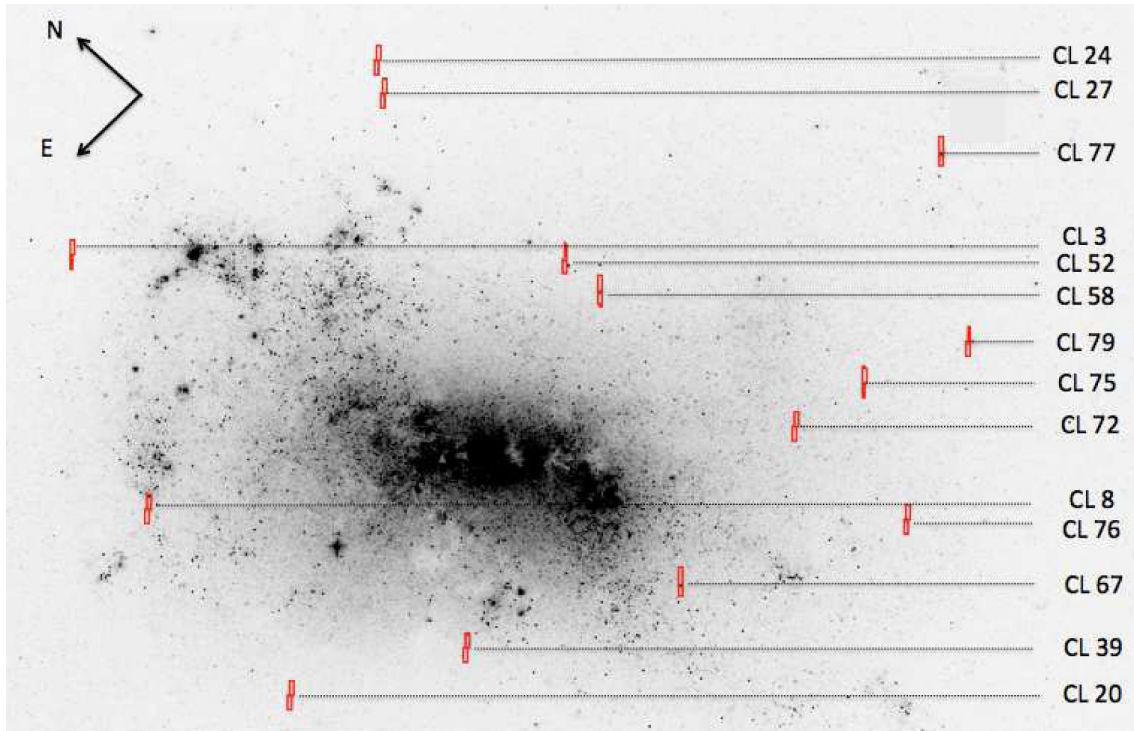


Figure 1. *HST*/ACS mosaic image of NGC 4449 in *F555W* ($\sim V$) with superimposed the LBT/MODS 1 arcsec \times 8 arcsec slits centred on star clusters. The cluster identification numbers correspond to those in Annibali et al. (2011b).

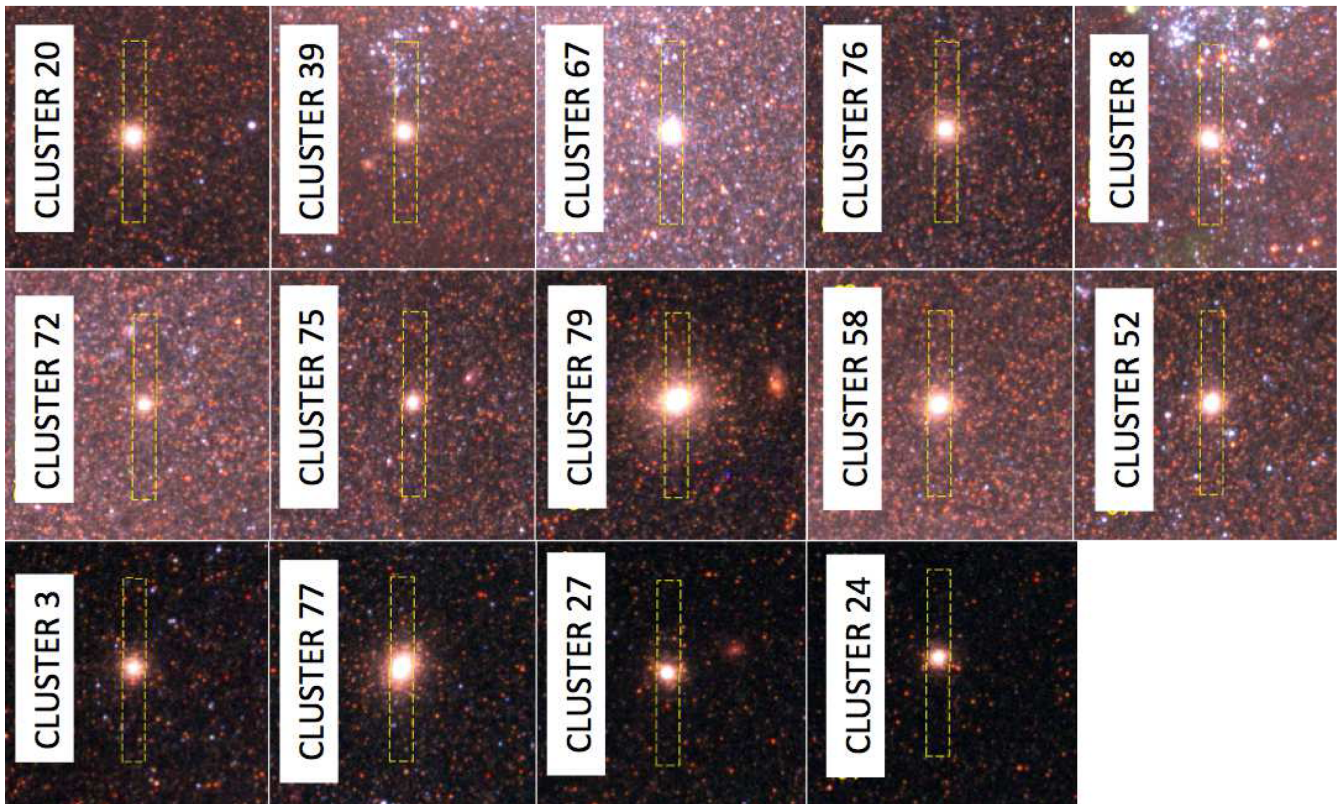


Figure 2. *HST*/ACS colour-combined images (*F435W* = blue, *F555W* = green, *F814W* = red) of clusters in NGC 4449 targeted for spectroscopy with LBT/MODS. In each box, the cluster identification number is that of *All*. Each field of view is 12 arcsec \times 12 arcsec, and the slit is 1 arcsec \times 8 arcsec.

Table 1. Journal of LBT/MODS observations for clusters in NGC 4449. Column (1): exposure number; column (2): date of observations; column (3): exposure time in seconds; column (4): average seeing in arcsec; column (5): average airmass; column (6): position angle in degree; column (7): parallactic angle in degree.

N.	Date-obs	Exp. time (s)	Seeing (arcsec)	Airmass	PosA	ParA
1	2013-01-20	1800	0.9	1.7	-35°	-78°
2	2013-01-20	1800	0.9	1.5	-35°	-83°
3	2013-01-20	1800	0.8	1.3	-35°	-88°
4	2013-01-20	1800	0.7	1.2	-35°	-93°
5	2013-01-21	1800	0.9	1.7	-35°	-76°
6	2013-01-21	1800	0.8	1.5	-35°	-81°
7	2013-01-21	1800	0.8	1.4	-35°	-86°
8	2013-01-21	1800	0.7	1.3	-35°	-91°

Table 2. Observed Lick standard stars. Lick standard stars were observed with a 1 arcsec \times 8 arcsec long slit. Column (1): star name; column (2): spectral type; column (3): date of observations; column (4): exposure time in seconds; column (5): V apparent magnitude.

Name	Spectral type	Date-obs	Exp. time (s)	V
HD 74377	K3 V	2013-01-20	1	8.2
HD 84937	F5 VI	2013-01-20	1	8.3
HD 108177	F5 VI	2013-01-21	1	9.7

INAF-IASF Milano, producing the calibrated two-dimensional (2D) spectra for the individual sub-exposures. The accuracy of the wavelength calibration obtained from the pipeline was checked against prominent sky lines adopting the nominal sky wavelengths tabulated in Hanuschik (2003). In fact, while arc lamps typically provide a good calibration of the wavelength variation with pixel position, a zero-point offset may be expected due to the fact that the light from the night sky and the light from the lamp do not follow the same path through the optics. In our case, we found that the $\Delta\lambda$ offset depended on slit position and was lower than $\sim 1 \text{ \AA}$ for both the blue and the red spectra; this zero-point correction was applied to our data.

Sky subtraction was performed on the 2D calibrated spectra; to this purpose, we used the *background* task in IRAF¹, typically choosing the windows at the two opposite sides of the cluster. This procedure does in principle remove, together with the sky, also the contribution from the NGC 4449’s unresolved background. In particular, the *background* subtraction should remove from the cluster spectra possible emission line contamination due to the presence of diffuse ionized gas in NGC 4449; however, as we will see in Section 3.3, the subtraction is not always perfect (e.g. because of the highly variable emission background) and some residual emission may still be present in some clusters after background subtraction. This is shown in Fig. 3, where we present the case of cluster CL 72 as an illustrative example. Here, the emission line spectrum is highly variable within the slit, preventing a perfect background removal; as a result, the final background-subtracted spectrum appears still contaminated by residual emission lines.

¹ IRAF is distributed by the National Optical Astronomy Observatory, which is operated by the Association of Universities for Research in Astronomy, Inc., under cooperative agreement with the National Science Foundation.

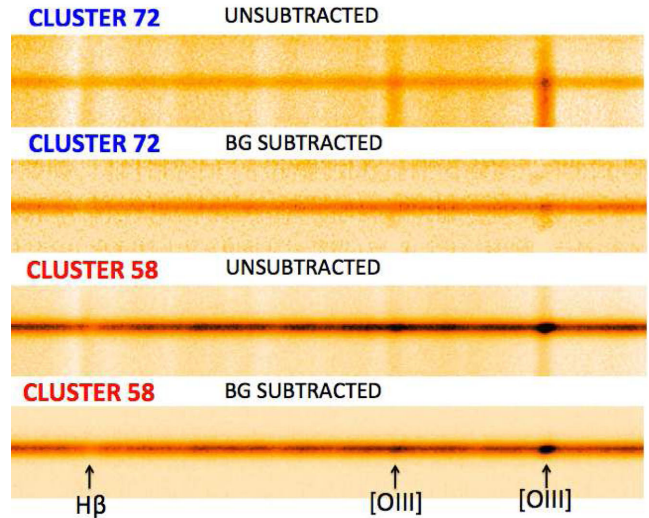


Figure 3. Two examples of cluster spectra contaminated by emission lines. Portions of the spectra around the $H\beta$ and $[O\text{ III}] \lambda\lambda 4959, 5007 \text{ \AA}$ lines are shown. For each cluster, the total combined unsubtracted spectrum is in the higher row, while the background-subtracted spectrum is just below. Cluster CL 72 suffers contamination from the diffuse ionized gas in NGC 4449, and some residual emission is still present after background subtraction. In cluster CL 58, the (modest) contamination from the diffuse ionized gas in NGC 4449 is optimally removed with the background subtraction; on the other hand, the cluster exhibits a quite strong centrally concentrated emission.

Ionized gas emission is detected in all the clusters of our sample except clusters CL 75, CL 79, and CL 77; as expected, the strongest emission is observed for the clusters located in the vicinity of star-forming regions, i.e. clusters CL 39, CL 67, and CL 8. Cluster CL 58 shows strong emission as well but, at variance with all the other clusters, its emission appears ‘nuclear’, i.e. confined within the cluster itself (see Fig. 3). We will come back to the case of cluster CL 58 later in Section 5.

We combined the sky-subtracted 2D spectra into a single frame for the blue and the red channels, respectively. The *apall* task in the *twodspec* IRAF package was then used to extract the 1D spectra from the 2D ones. In order to refine the emission subtraction, the *apall* task was run with the background subtraction option ‘on’. To derive the effective spectral resolution, we used the combined 1D spectra with no sky subtraction, and measured the full width at half-maximum (FWHM) of the most prominent sky lines; this resulted into resolutions of $R \sim 1040$ and $R \sim 1500$ at 4358 \AA and 7000 \AA , respectively.

The blue and red 1D spectra were flux calibrated using the sensitivity curves from the Italian LBT Spectroscopic Reduction pipeline; the curves were derived using the spectrophotometric standard star Feige 66 observed in dichroic mode with a 5-arcsec-wide slit on 2013 January 20. To obtain the red and blue sensitivity curves, the observed standard was compared with reference spectra in the *HST* CALSPEC data base. Atmospheric extinction corrections were applied using the average extinction curve available from the MODS calibration webpage at <http://www.astronomy.ohio-state.edu/MODS/Calib/>. As discussed in our study of $H\text{ II}$ regions and PNe in NGC 4449 based on LBT/MODS data acquired within run A of the same programme (Annibali et al. 2017), this may introduce an uncertainty in flux calibration as high as ~ 15 per cent below $\sim 4000 \text{ \AA}$.

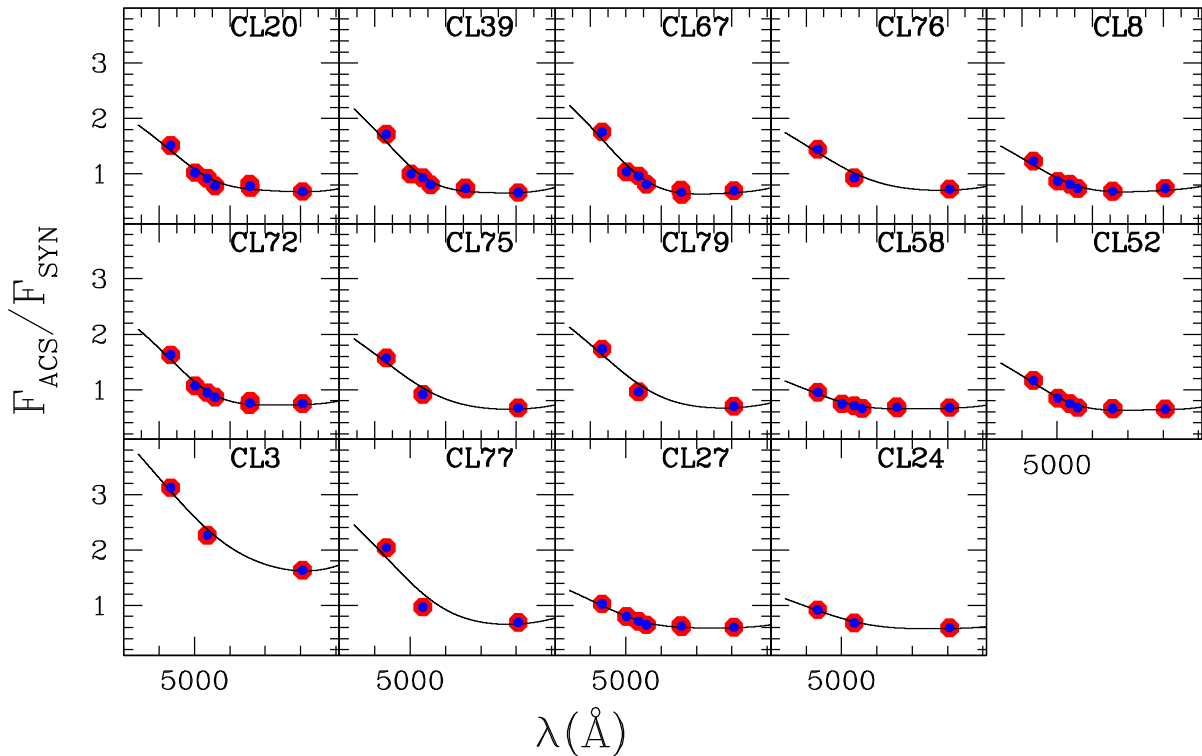


Figure 4. Effect of differential atmospheric refraction on our cluster spectroscopy. In ordinate, $F_{\text{ACS}}/F_{\text{SYN}}$ is the ratio between the measured ACS fluxes (in $F435W$, $F555W$, $F814W$, $F502N$, $F550M$, $F658N$, and $F660N$) and the SYNPHOT synthetic fluxes (see Section 2 for details). The curve is the fit obtained adopting a radial basis function (RBF).

2.1 Differential atmospheric refraction

Our observations were significantly affected by differential atmospheric refraction (Filippenko 1982) due to the displacement between the slit position angle and the parallactic angle, coupled with the relatively high airmass (see the journal of observations in Table 1). In order to quantify this effect as a function of wavelength, we used *HST*/ACS imaging in $F435W$ (B), $F555W$ (V), $F814W$ (I), and $F658N$ ($H\alpha$) from our GO programme 10585 and archive *HST*/ACS imaging in $F502N$ ($[\text{O III}]$), $F550M$, and $F660N$ ($H\alpha$) from GO programme 10522 (PI: Calzetti). The $F435W$, $F555W$, and $F814W$ images cover a field of view of $\sim 380 \text{ arcsec} \times 200 \text{ arcsec}$, obtained with two ACS pointings, while the $F502N$, $F550M$, $F660N$, and $F658N$ images have a smaller field of view of $\sim 200 \text{ arcsec} \times 200 \text{ arcsec}$. As a consequence, the most central clusters have photometric coverage in all seven bands, while more ‘peripheral’ ones (i.e. clusters CL 76, CL 75, CL 79, CL 3, CL 77, and CL 74) are detected only in B , V , and I . Aperture photometry of the clusters was performed on the ACS images with the *Polyphot* IRAF task adopting a polygonal aperture resembling the same aperture used to extract the 1D spectra from the 2D ones. Synthetic magnitudes in the same ACS filters were then derived with the *Calcphot* task in the *SYNPHOT* package by convolving the MODS spectra with the ACS bandpasses. Fig. 4 shows the ratio of the ACS fluxes over the synthetic *SYNPHOT* fluxes as a function of wavelengths. The fit to the data points was obtained adopting a radial basis function (RBF) available in PYTHON². Fig. 4 shows a

significant increase of the $F_{\text{ACS}}/F_{\text{SYN}}$ ratio towards bluer wavelengths, while the trend flattens out in the red. This behaviour translates into a loss of flux in the blue region of our spectra, as expected in the case of a significant effect from differential atmospheric refraction. We also notice that, at red wavelengths, the $F_{\text{ACS}}/F_{\text{SYN}}$ ratio is not equal to unity but lower than that, indicating that the fluxes from the spectra are overestimated. As discussed in Smith et al. (2007) and Annibali et al. (2017), flux calibrations are usually tied to reference point source observations, and therefore include an implicit correction for the fraction of the point source light that falls outside the slit; however, in the limit of a perfect uniform, slit-filling extended source, the diffractive losses out of the slit are perfectly balanced by the diffractive gains into the slit from emission beyond its geometric boundary; therefore, point-source-based calibrations likely cause an overestimate of the extended source flux. We used the curves obtained from the fits in Fig. 4 to correct our spectra; however, it is worth noticing that the line strength indices that will be used in Section 3 do not depend on absolute flux calibration (since they are normalized to local continua) and depend only very slightly on relative flux calibration as a function of wavelength.

2.2 Radial velocities

Radial velocities for the clusters were derived through the *fxcor* IRAF task by convolving the cluster spectra both with theoretical simple stellar populations (SSPs) and with observed stellar spectra. In the blue, the convolution was performed within the $\sim 3700\text{--}5500 \text{ \AA}$ range, masking, when present, emission lines; in the red, we used the Ca II triplet in the range $\sim 8000\text{--}8400 \text{ \AA}$. The velocities measured from the blue and red spectra present a systematic offset of $\lesssim 10 \text{ km s}^{-1}$, as shown in Fig. 5. This sets an upper limit to spurious

² RBF = $\sqrt{(r/\epsilon)^2 + 1}$, where r is the distance between any point and the centre of the basis function; see <http://docs.scipy.org/doc/scipy/reference/generated/scipy.interpolate.Rbf.html>.

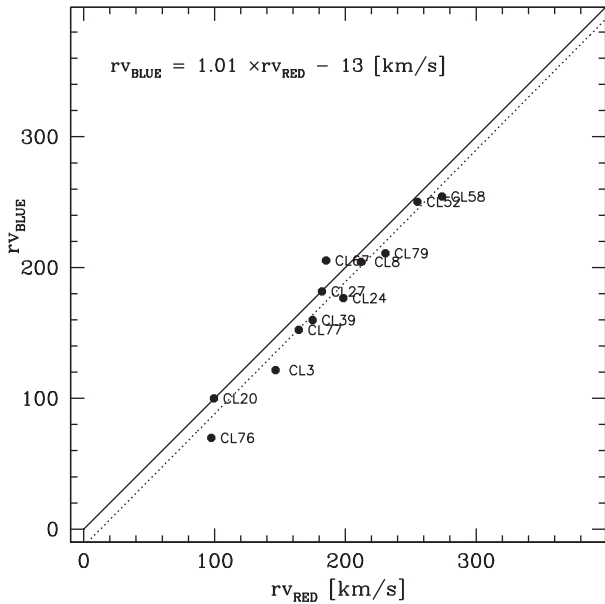


Figure 5. Comparison between cluster radial velocities obtained with the blue and with the red MODS spectra, respectively. The solid line is the one-to-one relation, while the dotted line is the linear fit to the data points. Notice that the displayed velocities have not been corrected here for the motion of around the Sun.

sources of error, such as the differential atmospheric refraction already discussed in Section 2.1: indeed, the fact that the clusters are miscentred in the slit as a function of wavelength causes also a small velocity shift. However, Fig. 5 demonstrates that this error is modest and that the derived velocities are suitable for a dynamical analysis (see Section 6). We find that the velocity uncertainties provided by the *fxcor* task are lower for the red than for the blue spectra, likely because of the higher signal-to-noise of the Ca II triplet lines compared to the lines used in the blue spectral region. Notice also that in general the Ca II triplet lines are easier to use for velocity measurements than blue lines, e.g. because they are less sensitive to template mismatch. Furthermore, they are better calibrated in wavelengths thanks to the wealth of sky lines in the red spectral region. For all these reasons, we elect hereafter the cluster velocities obtained from the Ca II triplet for our study.

The velocities are provided in Table 3. Corrections for the motion of around the Sun were performed with the *rvcorrect* task in IRAF. In addition, we provide radial velocities for the NGC 4449’s H II regions and PNe observed during run A. The H II region and PN velocities were derived from the most prominent emission lines, and also in this case the absolute wavelength calibration was anchored to strong sky lines observed in the spectra. The cluster radial velocities will be used in Section 6 to infer basic dynamical properties in NGC 4449.

2.3 Final spectra

The cluster spectra were transformed into the rest-frame system using the IRAF task *dpcor*. The final rest-frame, calibrated spectra in the blue and red MODS channels are shown in Figs 6–9.

3 NARROW-BAND INDICES

From the final calibrated spectra, we derived optical and near-infrared narrow-band indices that quantify the strength of stellar

Table 3. Heliocentric radial velocities of clusters, H II regions, and PNe in NGC 4449. Column (1): cluster, H II region, or PN identification; columns (2) and (3): right ascension and declination in J2000; column (4): heliocentric velocities in km s^{-1} .

Name	RA (J2000) (hh mm ss)	Dec. (J2000) (dd mm ss)	V_{helio} (km s^{-1})
CL 79	12 27 59.87	44 04 43.34	246 ± 15
CL 58	12 28 06.44	44 05 55.12	289 ± 14
CL 8	12 28 18.79	44 06 23.08	227 ± 20
CL76	12 28 03.88	44 04 15.26	113 ± 20
CL 67	12 28 09.34	44 04 38.99	201 ± 22
CL 39	12 28 14.60	44 05 00.43	190 ± 15
CL 20	12 28 18.82	44 05 19.61	115 ± 15
CL 52	12 28 06.64	44 06 07.78	270 ± 14
CL 3	12 28 16.44	44 07 29.49	162 ± 23
CL 77	12 27 57.53	44 05 28.16	180 ± 14
CL 27	12 28 07.72	44 07 13.42	197 ± 23
CL 24	12 28 07.32	44 07 21.54	214 ± 26
PN 1	12 28 04.126	44 04 25.14	225 ± 14
PN 2	12 28 03.540	44 04 34.80	196 ± 10
PN 3	12 28 03.972	44 05 56.78	173 ± 9
H II-1	12 28 12.626	44 05 04.35	191 ± 7
H II-2	12 28 09.456	44 05 20.35	168 ± 5
H II-3	12 28 17.798	44 06 32.49	225 ± 8
H II-4	12 28 16.224	44 06 43.32	218 ± 23
H II-5	12 28 13.002	44 06 56.38	217 ± 16
H II-6	12 28 13.925	44 07 19.04	232 ± 4

absorption lines with respect to local continua. More specifically, we computed the Lick indices in the optical (Worthey et al. 1994; Worthey & Ottaviani 1997), and the Ca II triplet index CaT* defined by Cenarro et al. (2001a, 2009).

3.1 Lick indices

For the computation of the Lick indices, the adopted procedure is the same as described in our previous papers (e.g. Rampazzo et al. 2005; Annibali et al. 2011a). Because of the low MODS sensitivity in the $\sim 5500\text{--}5800 \text{ \AA}$ range (see Section 2), the Lick indices Fe5709, Fe5781, NaD, TiO₁, and TiO₂ were not considered in our study. The MODS spectra were first degraded to match the wavelength-dependent resolution of the Lick–IDS system (FWHM $\sim 8.4 \text{ \AA}$ at 5400 \AA versus a MODS resolution of FWHM $\sim 5 \text{ \AA}$ at the same wavelength) by convolution with a Gaussian kernel of variable width. Then, the indices were computed on the degraded MODS spectra using the refined passband definitions of Trager et al. (1998). In order to calibrate the ‘raw’ indices into the Lick–IDS system, we used the three Lick standard stars (HD 74377, HD 84937, HD 108177) observed during our run with the same $1 \text{ arcsec} \times 8 \text{ arcsec}$ slit used for the clusters. Following the prescription by Worthey & Ottaviani (1997), we degraded the standard star spectra to the Lick resolution, computed the indices, and compared our measurements with the values provided by Worthey et al. (1994) to derive linear transformations in the form $EW_{\text{Lick}} = \alpha EW_{\text{raw}} + \beta$, where EW_{raw} and EW_{Lick} respectively are the raw and the calibrated indices, and α and β are the coefficients of the linear transformation. The transformations were derived only for those indices with three Lick star measurements,³ while we discarded the remaining ones

³ Tabulated index values for Lick standard stars can be found at <http://astro.wsu.edu/worthey/html/system.html>.

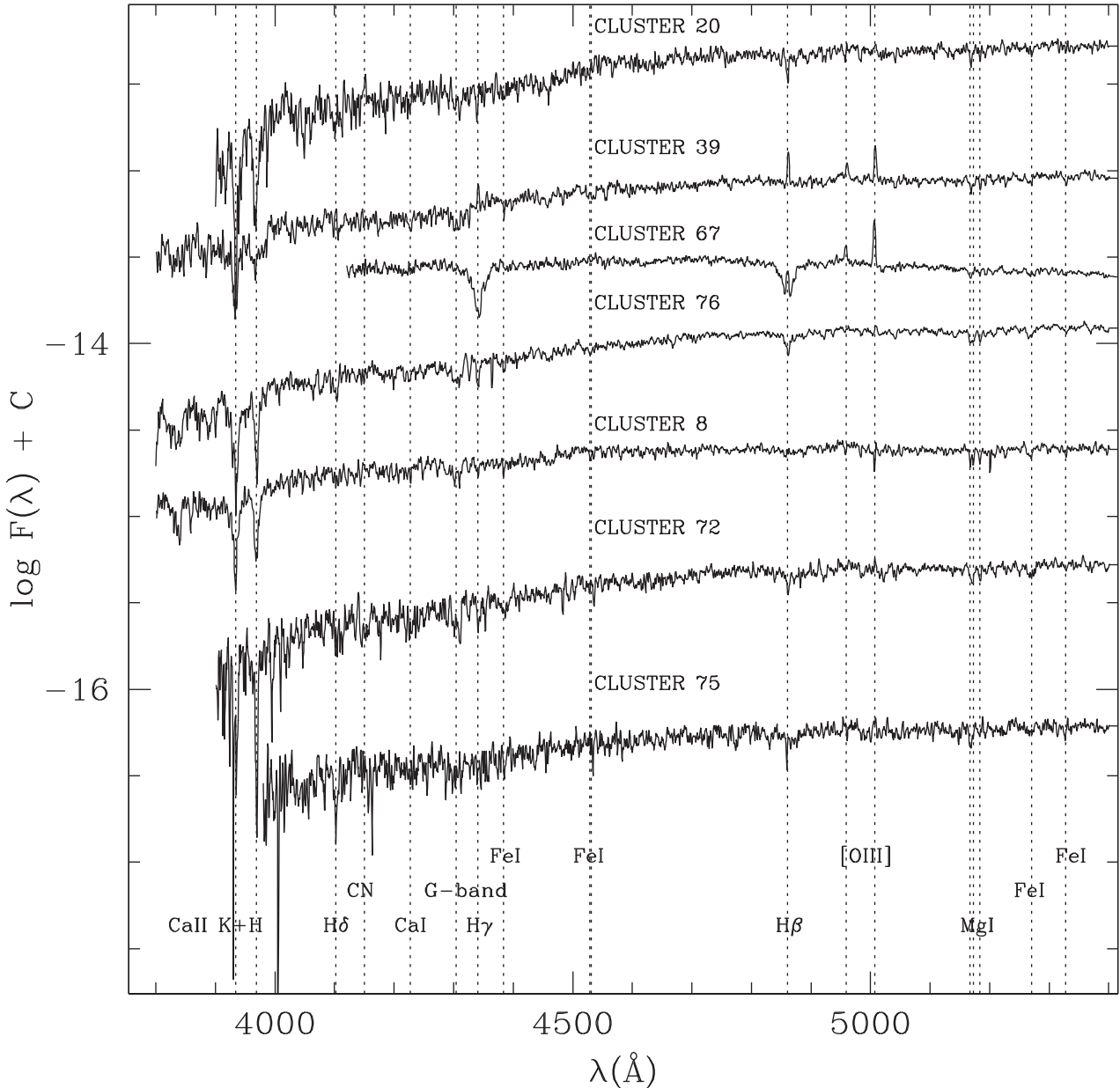


Figure 6. LBT/MODS blue calibrated spectra in the rest frame for clusters CL 20, CL 39, CL 67, CL 76, CL 8, CL 72, and CL 75 in NGC 4449. Indicated are the most prominent absorption and emission lines.

from our study. In the end, we were left with 18 out of the 25 Lick indices defined by Worthey et al. (1994) and Worthey & Ottaviani (1997): CN₁, CN₂, Ca4227, G4300, Fe4383, Ca4455, Fe4531, C₂4668, H β , Fe5015, Mg₁, Mg₂, Mgb, Fe5270, Fe5335, Fe5406, H γ A, and H γ F. The linear transformations, which are shown in Fig. 10 and Table 4, are consistent with small zero-point offsets for the majority of indices. No correction due to the cluster velocity dispersion was applied: in fact, while this is an important effect in the case of integrated galaxy indices, it is reasonable to neglect this correction for stellar clusters. The errors on the indices were determined through the following procedure. Starting from each cluster spectrum, we generated 1000 random modifications by adding a wavelength-dependent Poissonian fluctuation corresponding to the spectral noise. Then we repeated the index computation procedure on each ‘perturbed’ spectrum and derived the standard deviation. To these errors, we added in quadrature the errors on the

emission corrections (see Section 3.3) and the scatter around the derived transformations to the Lick systems (see Table 4).

3.2 Near-infrared indices

In the near-infrared, the Ca II triplet ($\lambda\lambda$ 8498, 8542, 8662 Å) is the strongest feature observed. Intermediate-strength atomic lines of Fe I ($\lambda\lambda$ 8514, 8675, 8689, 8824 Å), Mg I (λ 8807 Å), and Ti I (λ 8435 Å) are also present. The Paschen series is apparent in stars hotter than G3 and can significantly contaminate the measurement of the Ca II triplet. In order to overcome this problem, Cenarro et al. (2001a) defined a new Ca II triplet index, named CaT*, which is corrected from the contamination of the Paschen series. Adopting their definition, we computed the CaT* for our clusters in NGC 4449. In order to match the lower resolution of our spectra (FWHM \sim 5 Å in

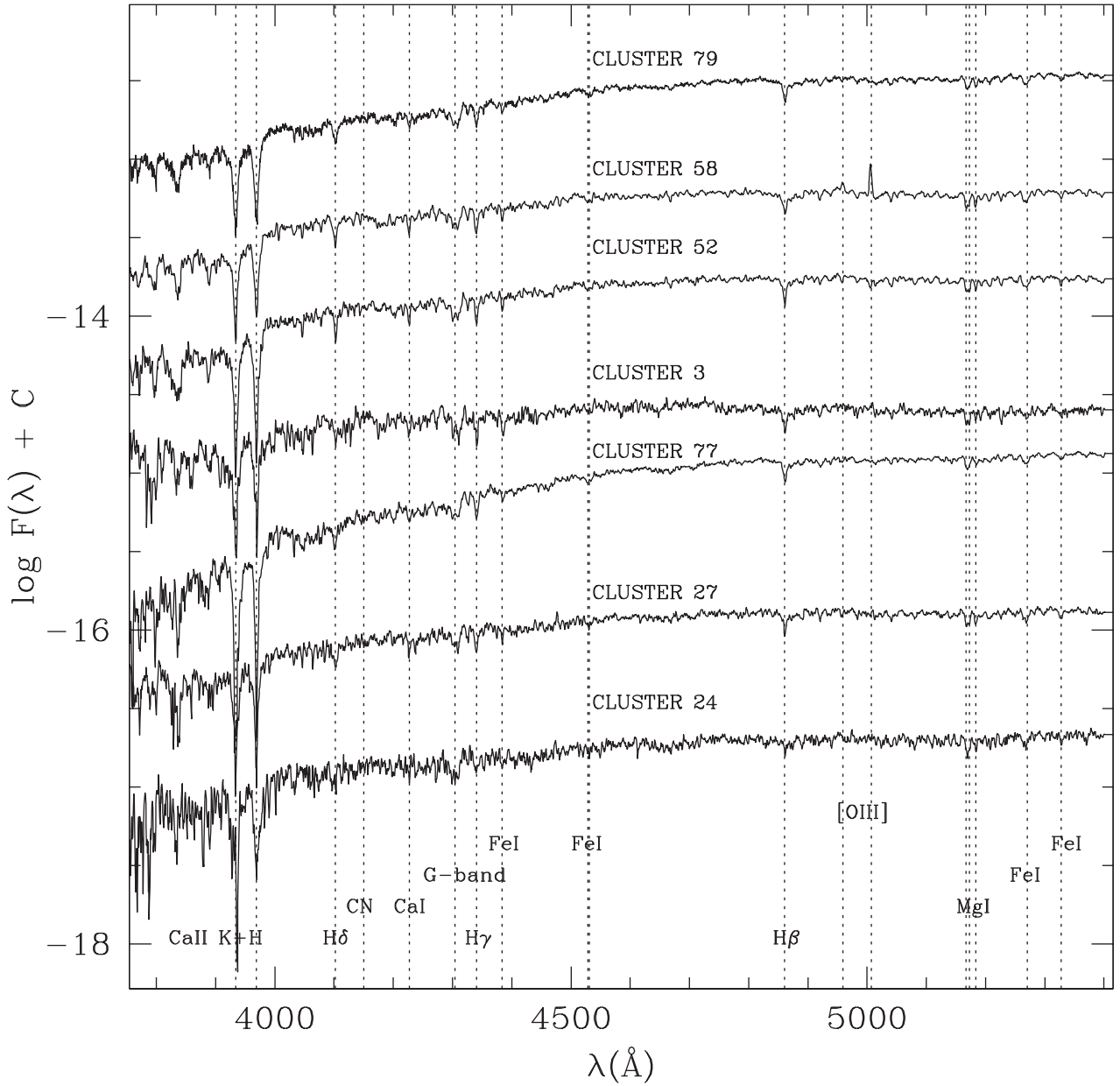


Figure 7. Same as in Fig. 6 but for clusters CL 79, CL 58, CL 52, CL 3, CL 77, CL 27, and CL 24.

the near-infrared) to the better resolution of the stellar library used by Cenarro et al. (2001a, FWHM \sim 1.5 Å), we used the prescriptions by Vazdekis et al. (2003). We did not consider the Mg I and sTiO indices defined by Cenarro et al. (2009), since these turned out to be highly affected by a large spectral noise due to the difficulty in subtracting the near-infrared sky background in our spectra (see Figs 8 and 9).

3.3 Emission contamination

As discussed in Section 2, the majority of our spectra suffer contamination from the diffuse ionized gas present in NGC 4449 and the removal of the emission line contribution obtained with the background subtraction is not always satisfactory. Even small amounts of contamination from ionized gas can have a significant impact on the derived integrated ages (Sereno & Worthey 2010; Concas et al.

2017): the effect of emission is to fill in and weaken the absorption Balmer lines, resulting into apparent older integrated ages. Figs 6–9 show the presence of residual emission in clusters CL 20, CL 39, CL 67, CL 76, CL 8, CL 72, CL 58, and CL 27. The remaining cluster spectra (CL 75, CL 79, CL 52, CL 3, CL 77, CL 24) can reasonably be considered emission-free.

We derived a correction to the Balmer absorption indices H β and H γ (the H δ indices were not used, as discussed in Section 3.1) for clusters CL 20, CL 67, CL 76, CL 72, CL 58, and CL 27, while the emission was too high in clusters CL 39 and CL 8 to attempt a recovery of the true absorption lines. We used the *deblend* function in the *splot* IRAF task to measure the flux of the [O III] λ 5007 emission line; then, we used the relation between the [O III] and the H β fluxes to compute the correction to the Balmer indices. It is well known that the $F_{[\text{O III}]} / F_{\text{H}\beta}$ ratio is subject to a large dispersion, since it strongly depends on the properties of the ionized gas. To overcome

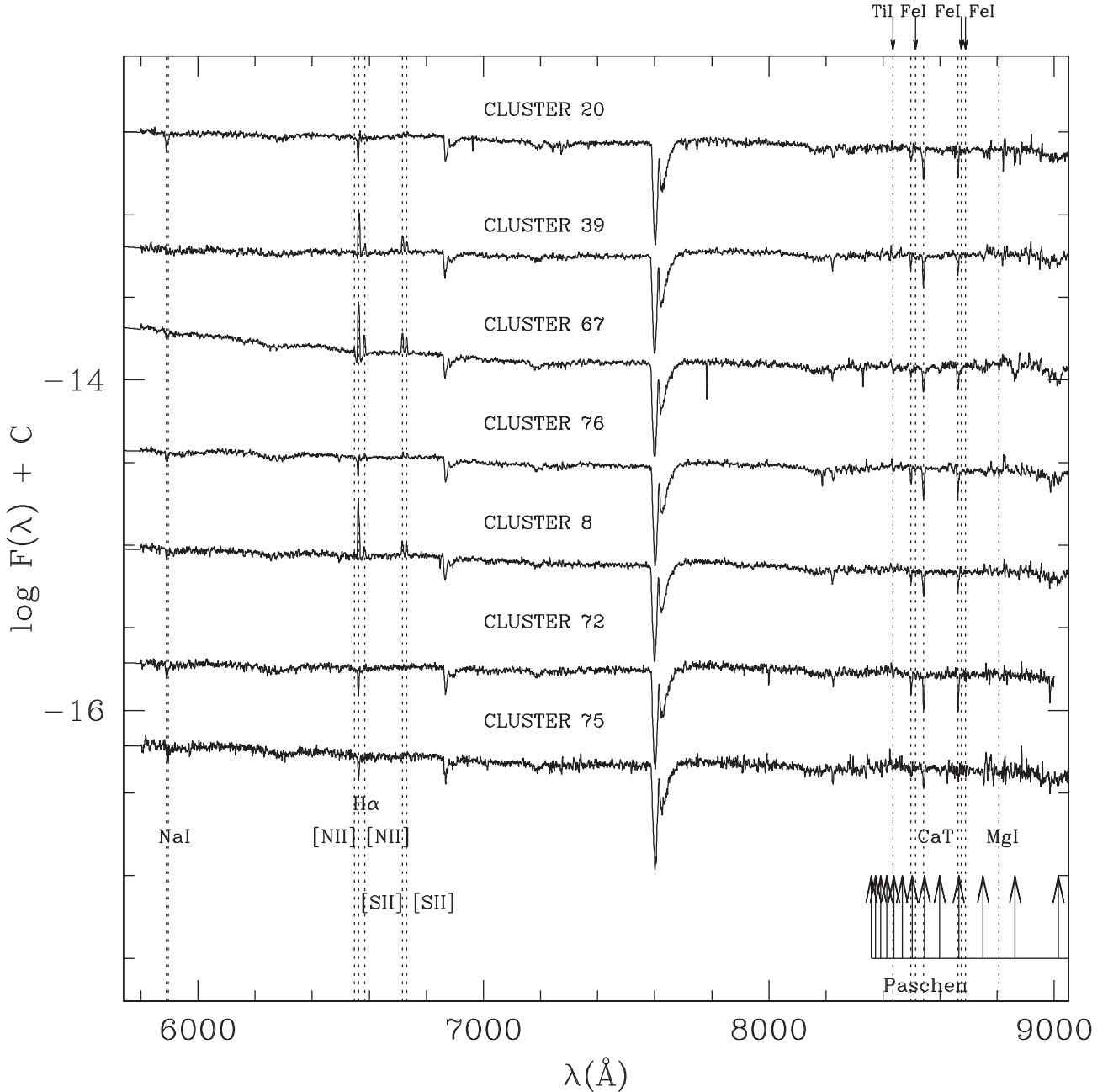


Figure 8. LBT/MODS red calibrated spectra in the rest frame for clusters CL 20, CL 39, CL 67, CL 76, CL 8, CL 72, and CL 75 in NGC 4449. Indicated are the most prominent absorption and emission lines.

this difficulty and properly correct our data, we used the results from our study of the H II regions in NGC 4449 (Annibali et al. 2017): from the six H II regions analysed, we obtain an average flux ratio of

$$\frac{F_{[\text{O III}]}}{F_{\text{H}\beta}} = 3.2 \pm 0.7, \quad (1)$$

from which the H β emission can be derived. For H II regions with temperature $T_e = 10\,000\text{ K}$ and density $n_e = 100\text{ cm}^{-3}$, the H γ emission is obtained from the theoretical relations of Storey & Hummer (1995), once the H β flux is known:

$$\frac{F_{\text{H}\gamma}}{F_{\text{H}\beta}} \sim 0.47. \quad (2)$$

In the end, we computed the corrections to the Balmer indices by normalizing the $F_{\text{H}\gamma}$ and $F_{\text{H}\beta}$ fluxes to the ‘pseudo-continua’ defined in the Lick system. The uncertainties on the corrections were computed by propagating both the errors on the measured fluxes and the dispersion in equation (1). Our results are summarized in Table 5. We caution that the adopted emission line ratios may not be appropriate for cluster CL 58, where the emission source could be different from an H II region. For instance, if the emission lines were due to the presence of a PN, a more adequate ratio would be $F_{[\text{O III}]5007}/F_{\text{H}\beta} \sim 10$ (Annibali et al. 2017), resulting into lower Balmer corrections than those listed in Table 5. For this reason, we will consider the final corrected Balmer line strengths for cluster CL 58 as upper limits.

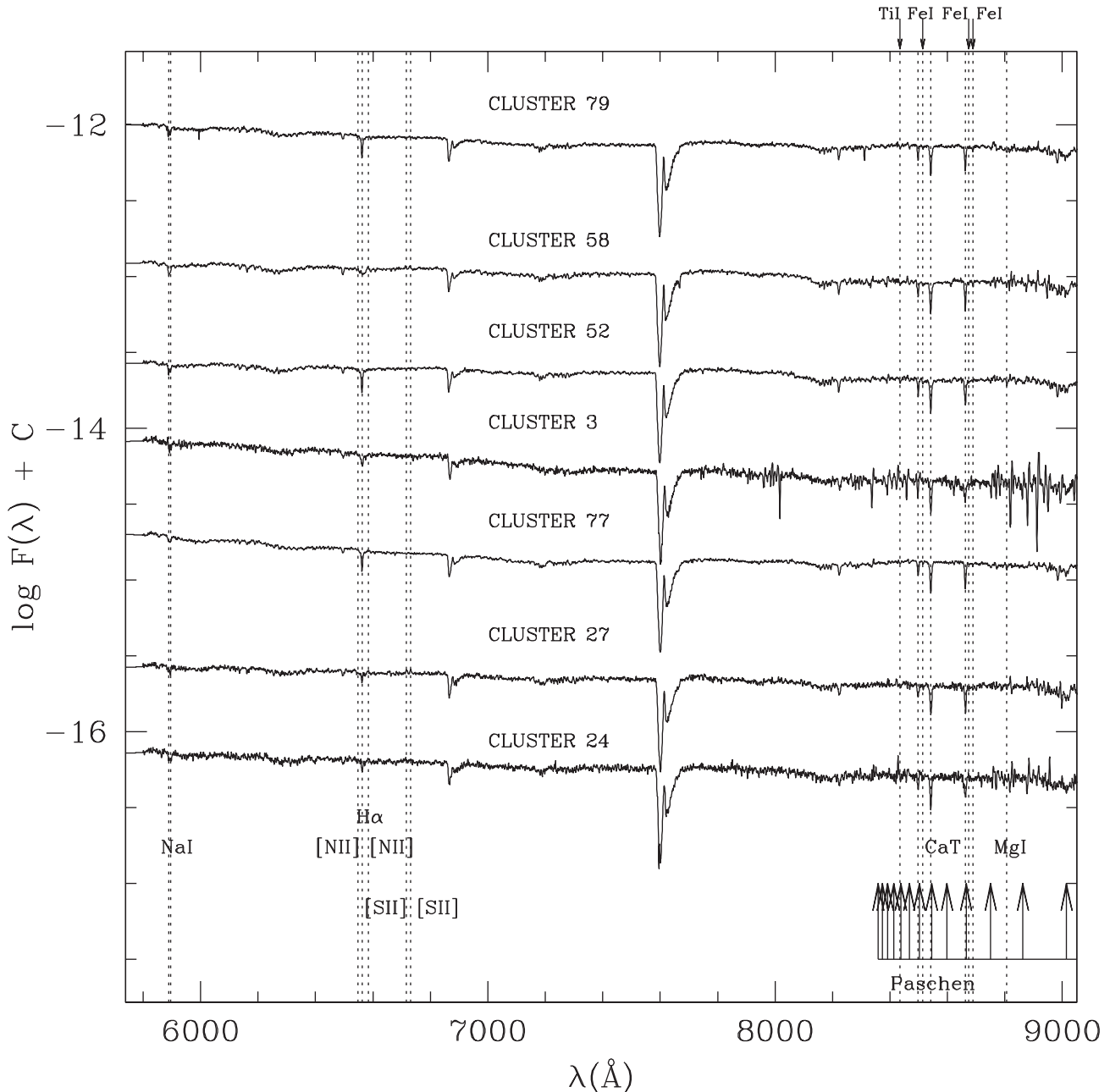


Figure 9. Same as in Fig. 8 but for clusters CL 79, CL 58, CL 52, CL 3, CL 77, CL 27, and CL 24.

For cluster CL 67, we could also directly derive the emission in $H\beta$ and $H\alpha$ by fitting the observed spectrum with combinations of Voigt profiles (in absorption) plus Gaussian profiles (in emission; see Annibali et al. 2017, for a similar case). This allowed us to perform a consistency check of our procedure. From Table 5, we get $F_{H\alpha}/F_{H\beta} = 2.97 \pm 0.11$, in agreement with the theoretical value of ~ 2.86 for $H II$ regions (Osterbrock 1989; Storey & Hummer 1995). Furthermore, equation (1) provides an emission in $H\beta$ of $(10 \pm 2) \times 10^{-17} \text{ erg s}^{-1} \text{ cm}^{-2}$, marginally consistent with the value of $(14.5 \pm 0.4) \times 10^{-17} \text{ erg s}^{-1} \text{ cm}^{-2}$ derived from the direct spectral fit. Notice that for cluster CL 67 the corrections provided in Table 5 are those obtained from the direct spectral fit. The final corrected indices are provided in Table A1 in Appendix.

4 STELLAR POPULATION PARAMETERS FOR CLUSTERS IN NGC 4449

In Figs 11–14, we compare the indices derived for the NGC 4449’s clusters with our set of SSP models (Annibali et al. 2007, 2011a). The models are based on the Padova SSPs (Bressan, Chiosi & Fagotto 1994, and references therein), and on the fitting functions (FFs) of Worthey et al. (1994) and Worthey & Ottaviani (1997). The SSPs were computed for different element abundance ratios, where the departure from the solar-scaled composition is based on the index responses by Korn, Maraston & Thomas (2005). In the models displayed in Figs 11–13, the elements O, Ne, Na, Mg, Si, S, Ca, and Ti are assigned to the α -element group, and Cr, Mn, Fe, Co, Ni, Cu, and Zn to the Fe-peak group. We assume that the elements within

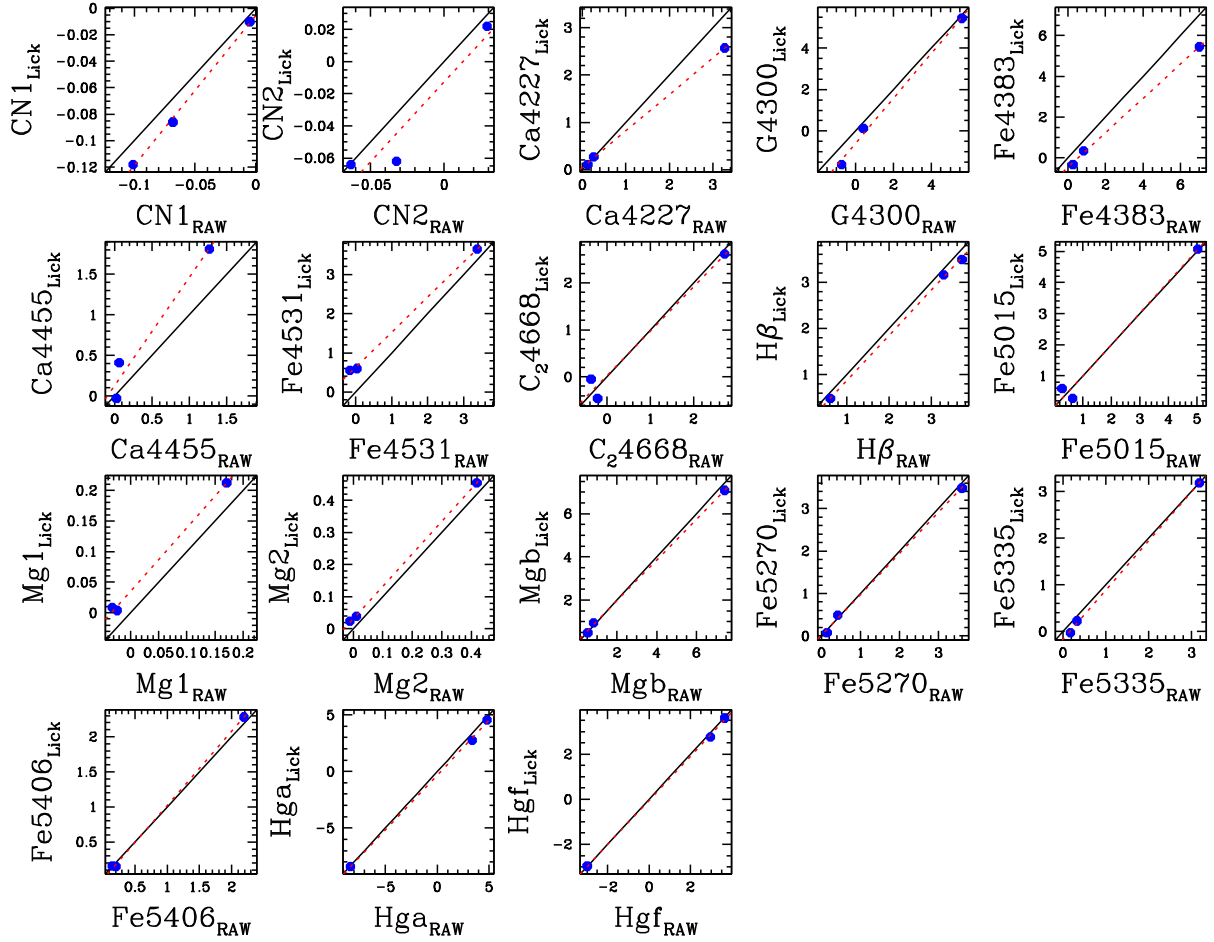


Figure 10. Comparison between the nominal Lick index values and our measurements for the three Lick standard stars (HD 74377, HD 84937, and HD 108177) observed during our run. The solid line is the one-to-one relation, while the dotted line is the least-squares linear fit.

Table 4. Linear transformations to the Lick–IDS system. a and b are the coefficients of the transformation $EW_{\text{Lick}} = \alpha EW_{\text{raw}} + \beta$, where EW_{raw} and EW_{Lick} respectively are the raw and the calibrated indices; rms is the root-mean-square deviation around the best linear fit.

Index	Unit	a	b	rms
CN ₁	mag	1.13 ± 0.06	-0.005 ± 0.004	0.002
CN ₂	mag	1.0 ± 0.3	-0.01 ± 0.01	0.01
Ca4227	Å	0.77 ± 0.01	0.04 ± 0.03	0.02
G4300	Å	1.09 ± 0.08	-0.6 ± 0.3	0.2
Fe4383	Å	0.84 ± 0.02	-0.5 ± 0.1	0.07
Ca4455	Å	1.3 ± 0.3	0.1 ± 0.2	0.2
Fe4531	Å	0.89 ± 0.03	0.63 ± 0.06	0.05
C ₂ 4668	Å	0.9 ± 0.2	0.0 ± 0.2	0.2
H β	Å	0.98 ± 0.03	-0.11 ± 0.08	0.04
Fe5015	Å	1.1 ± 0.1	0.0 ± 0.4	0.3
Mg ₁	mag	1.03 ± 0.06	0.035 ± 0.006	0.006
Mg ₂	mag	1.01 ± 0.01	0.032 ± 0.004	0.003
Mgb	Å	0.94 ± 0.02	0.1 ± 0.1	0.07
Fe5270	Å	0.96 ± 0.03	0.01 ± 0.07	0.05
Fe5335	Å	1.05 ± 0.03	-0.16 ± 0.05	0.04
Fe5406	Å	1.06 ± 0.03	-0.03 ± 0.03	0.02
H γ A	Å	0.97 ± 0.02	-0.3 ± 0.1	0.1
H γ F	Å	0.98 ± 0.02	-0.05 ± 0.07	0.07

one group are enhanced/depressed by the same factor; the α and Fe-peak elements are respectively enhanced and depressed in the $[\alpha/\text{Fe}] > 0$ models, while the opposite holds for the $[\alpha/\text{Fe}] < 0$ models. Other elements, such as N and C, are left untouched and scale with the solar composition. We caution that all these assumptions are an oversimplification: in fact, recent studies suggest that Mg possibly behaves differently from the other α 's (see Pancino et al. 2017, their section 4.3), and it is well known that Galactic globular clusters (GCs) exhibit an anti-correlation between Na and O, and between C and N (e.g. Carretta et al. 2006); an anti-correlation between Mg and Al has also been observed for the most metal-poor and/or most massive GCs (Pancino et al. 2017). Furthermore, notice that the stellar evolutionary tracks adopted in our models have solar-scaled chemical compositions (Fagotto et al. 1994a,b) and that only the effect due to element abundance variations in the model atmospheres, as quantified by the Korn et al. (2005) response functions, is included.

In Figs 11–13, we plot the Lick indices for our clusters against the metallicity-sensitive $[\text{MgFe}]'$ index⁴, which presents the advantage of being mostly insensitive to Mg/Fe variations (González 1993; Thomas, Maraston & Bender 2003). For comparison, we also show the indices derived by Puzia et al. (2002) for Galactic clusters in

⁴ Defined as $[\text{MgFe}]' = \sqrt{\text{Mgb} \times (0.72 \cdot \text{Fe5270} + 0.28 \cdot \text{Fe5335})}$.

Table 5. Emission lines and corrections to the Balmer indices. Column (1): cluster name; columns (2)–(4): measured fluxes for [O III], H β , and H α in emission; columns (5) and (6): correction to be applied to the H γ and H β absorption indices.

Cluster ID	$F[\text{O III}]$ ($\text{erg s}^{-1} \text{cm}^{-2} 10^{-17}$)	$F\text{H}\beta$ ($\text{erg s}^{-1} \text{cm}^{-2} 10^{-17}$)	$F\text{H}\alpha$ ($\text{erg s}^{-1} \text{cm}^{-2} 10^{-17}$)	$\Delta\text{EW}_{\text{H}\gamma}$ (\AA)	$\Delta\text{EW}_{\text{H}\beta}$ (\AA)
CL 20	1.8 ± 0.2	–	–	0.15 ± 0.04	0.19 ± 0.05
CL 67	32.7 ± 0.2	14.5 ± 0.4	43 ± 1	0.78 ± 0.02	1.67 ± 0.04
CL 76	2.0 ± 0.1	–	–	0.08 ± 0.02	0.11 ± 0.02
CL 58	27.9 ± 0.2	–	–	0.4 ± 0.1	0.7 ± 0.2
CL 72	1.3 ± 0.1	–	–	0.13 ± 0.03	0.18 ± 0.04
CL 27	0.77 ± 0.08	–	–	0.04 ± 0.01	0.06 ± 0.01

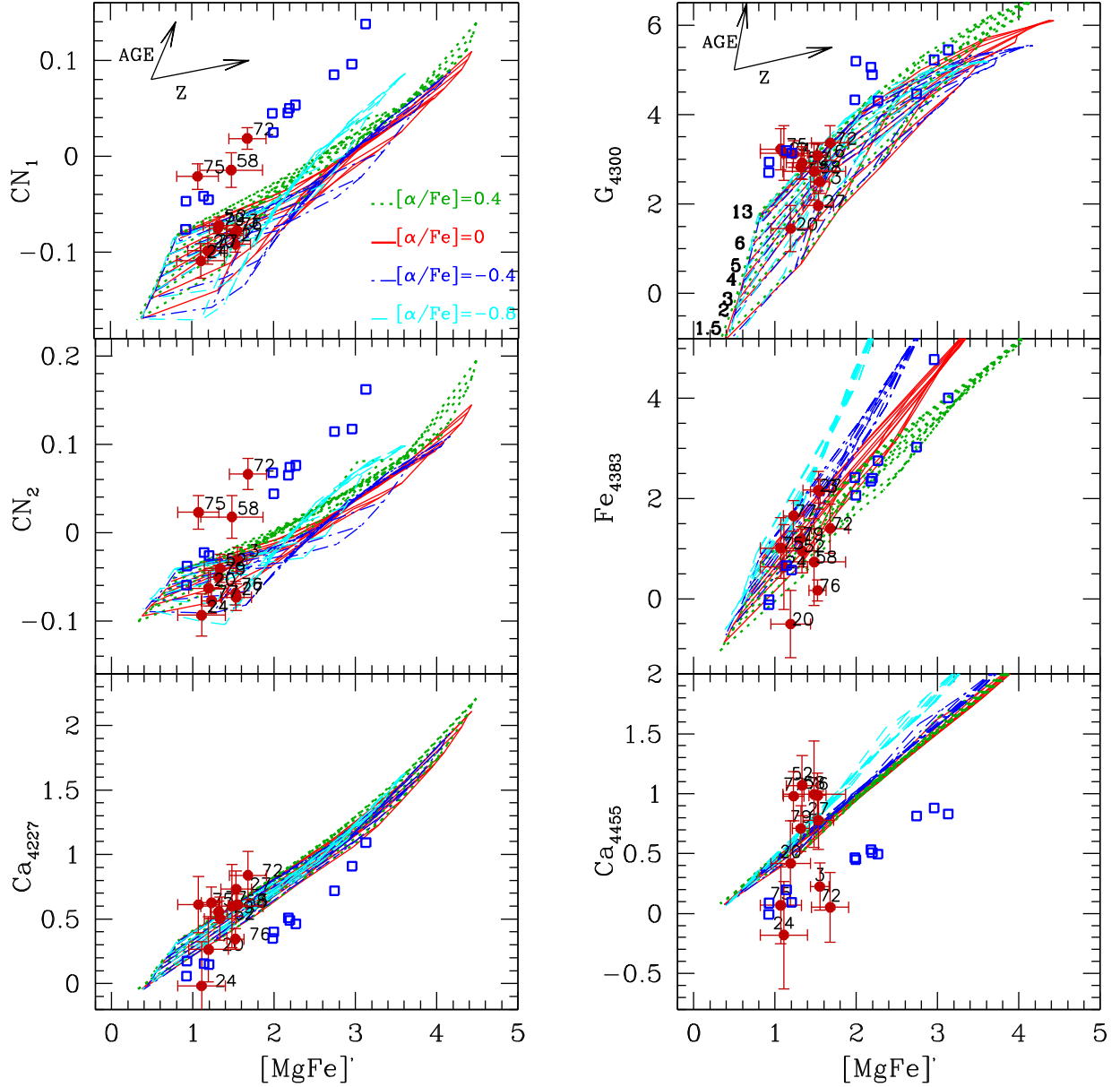


Figure 11. Comparison of cluster Lick indices (CN_1 , CN_2 , Ca_{4227} , G_{4300} , Fe_{4383} , Ca_{4455} versus $[\text{MgFe}]'$) with our SSP models. The filled red circles are the NGC 4449 clusters from this work, while the open blue squares are the MW halo and bulge globular clusters from Puzia et al. (2002). The displayed models are for metallicities $Z = 0.0004, 0.004, 0.008, 0.02, 0.005$, ages from 1 to 13 Gyr, and $[\alpha/\text{Fe}] = -0.8, -0.4, 0$, and 0.4 .

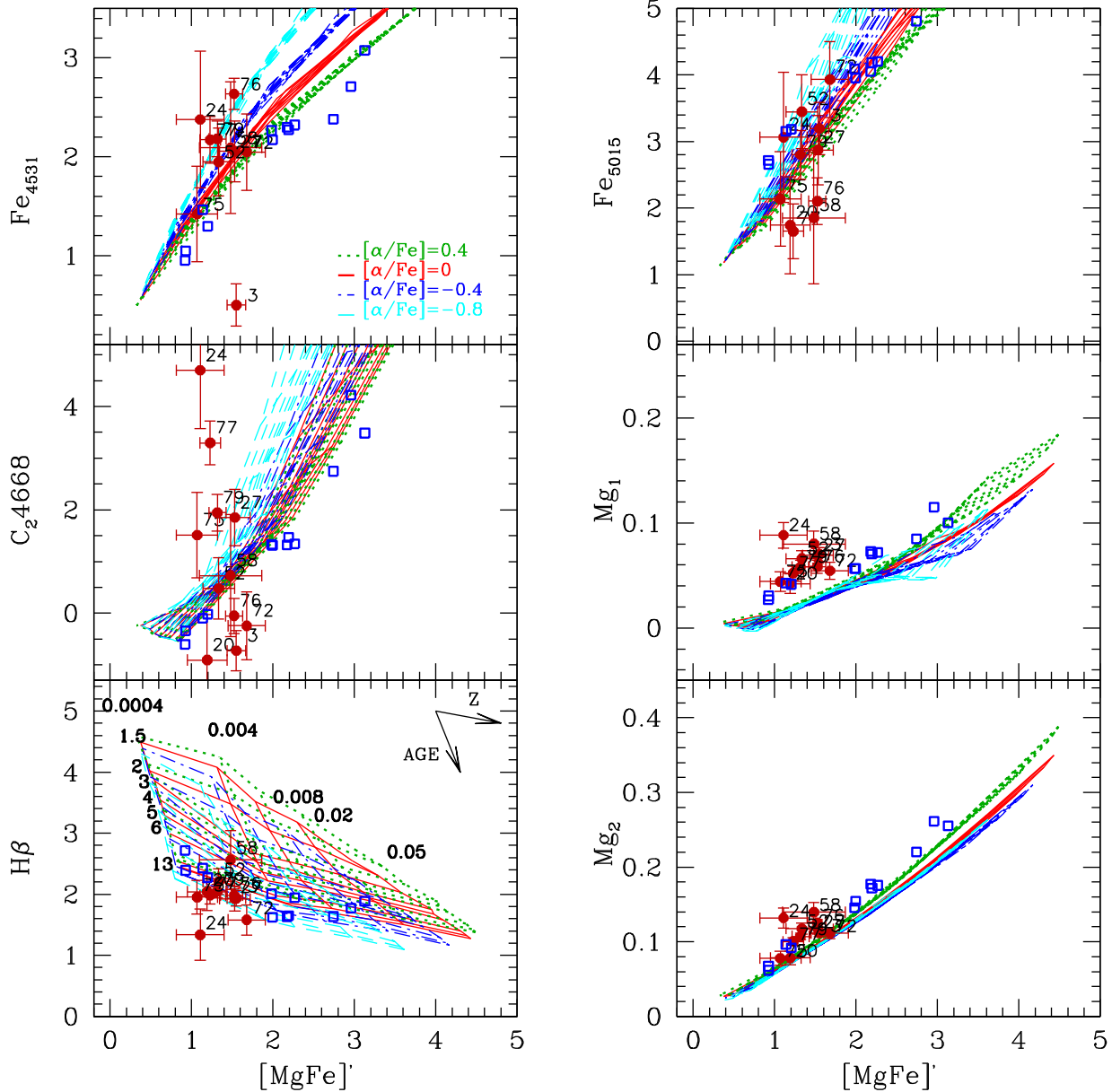


Figure 12. Same as in Fig. 11 but for the Lick indices Fe_{4531} , C_{24668} , $H\beta$, Fe_{5015} , Mg_1 , and Mg_2 . The metallicity and age labels (Z and Gyr, respectively) refer to the $[\alpha/Fe] = 0$ models.

the halo and in the bulge. In Fig. 14, NGC 4449’s clusters are plotted instead on optical–near-infrared planes, with a Lick index versus CaT^* ; here the models have solar-scaled composition since, to our knowledge, specific responses of the CaT^* index to individual element abundance variations have not been computed yet.

4.1 Discussion on individual indices

The CN_1 and CN_2 indices measure the strength of the CN absorption band at ~ 4150 Å, and exhibit a strong positive response to the abundances of C and N. On the other hand, they are almost insensitive to $[\alpha/Fe]$ variations. In Fig. 11, the bulk of clusters in NGC 4449 nicely overlaps the SSP models. The Milky Way (MW) clusters, instead, exhibit a significant offset from the models, a behaviour that has been explained as due to a significant nitrogen enhancement (e.g. Origlia, Rich & Castro 2002; Puzia et al. 2002; Thomas, Maraston

& Bender 2003). Three clusters in our sample, namely CL 72, CL 75, and CL 58, occupy the same high CN strength region of the Galactic GCs. In order to match the Puzia et al. (2002) Galactic GC data with their SSP models, Thomas et al. (2003) needed to assume $[N/\alpha] = 0.5$ (i.e. a factor of 3 enhancement in nitrogen with respect to the α -elements). Notice that the CN features of the Galactic bulge are instead perfectly reproduced by models without N enhancement (Thomas et al. 2003). We will come back to the problem of the N abundance in NGC 4449’s clusters later in this paper.

The Ca_{4227} index is dominated by the Ca_{4227} absorption line, strongly correlates with metallicity, and, interestingly, is the only index besides CN_1 and CN_2 to be affected by changes in the C and N abundances (i.e. it anti-correlates with CN). While the MW GCs are shifted to lower Ca_{4227} values compared to the models [a discrepancy that according to Thomas et al. (2003) can be reconciled assuming $[N/\alpha] = 0.5$ models], the NGC 4449 clusters agree pretty

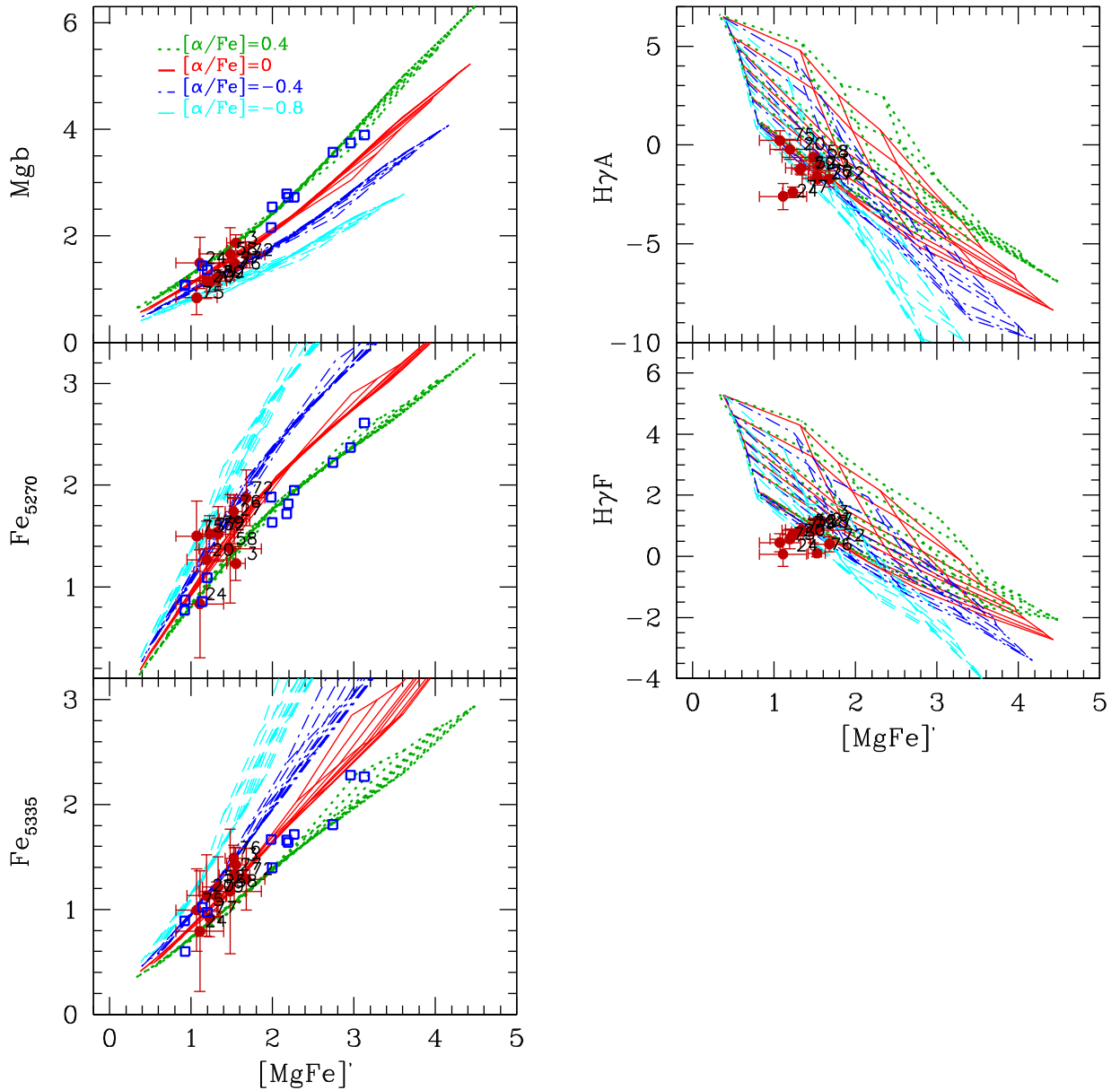


Figure 13. Same as in Fig. 11 but for the Lick indices Mgb, Fe5270, Fe5335, H γ A, and H γ F.

well with the SSPs. This behaviour is in agreement with the good match between data and models in the CN₁ and CN₂ indices. The **Ca4455** index, on the other hand, is not a useful abundance indicator. In fact, despite its name, it is a blend of many elements, and it has been shown to be actually insensitive to Ca (Tripicco & Bell 1995; Korn et al. 2005). It exhibits a very small dependence on the $[\alpha/\text{Fe}]$ ratio. Our data are highly scattered around the models, with quite large errors on the index measurements. Hereafter, we will not consider this index for our cluster stellar population analysis.

The **G4300** index measures the strength of the *G* band and is highly sensitive to the CH abundance. It exhibits a dependence on both age and metallicity, and no significant sensitivity to the $[\alpha/\text{Fe}]$ ratio, so that the G4300 versus $[\text{MgFe}]'$ plane can be used to separate age and metallicity to some extent. According to Fig. 11, our clusters have metallicities $Z \lesssim 0.004$ and ages in the ~ 3 –13 Gyr range. However, Thomas et al. (2003) noticed that the calibration of this index versus Galactic GC data is not convincing; therefore,

it is not clear if G4300 can provide reliable results on the stellar population properties.

The **C₂4668** index, formerly called Fe4668, is slightly sensitive to Fe and most sensitive to C abundance. It exhibits a low negative correlation with the $[\alpha/\text{Fe}]$ ratio. The NGC 4449 clusters data are highly scattered in the C₂4668 versus $[\text{MgFe}]'$ plane, possibly as a consequence of the large error in the C₂4668 measurement. As discussed by Thomas et al. (2003), this index is not well calibrated against Galactic GC data and therefore is not well suited for element abundance studies.

Among the indices that quantify the strength of Fe lines, **Fe5270** and **Fe5335** are the ones most sensitive to $[\alpha/\text{Fe}]$ variations. The other **Fe4383**, **Fe4531**, and **Fe5015** indices contain blends of many metallic lines other than Fe (e.g. Ti I, Ti II, Ni I) and may be less straightforward than Fe5270 and Fe5335 to interpret. Fig. 13 shows that models of different $[\alpha/\text{Fe}]$ ratios are very well separated in the Fe5270, Fe5335 versus $[\text{MgFe}]'$ planes, with the NGC 4449's

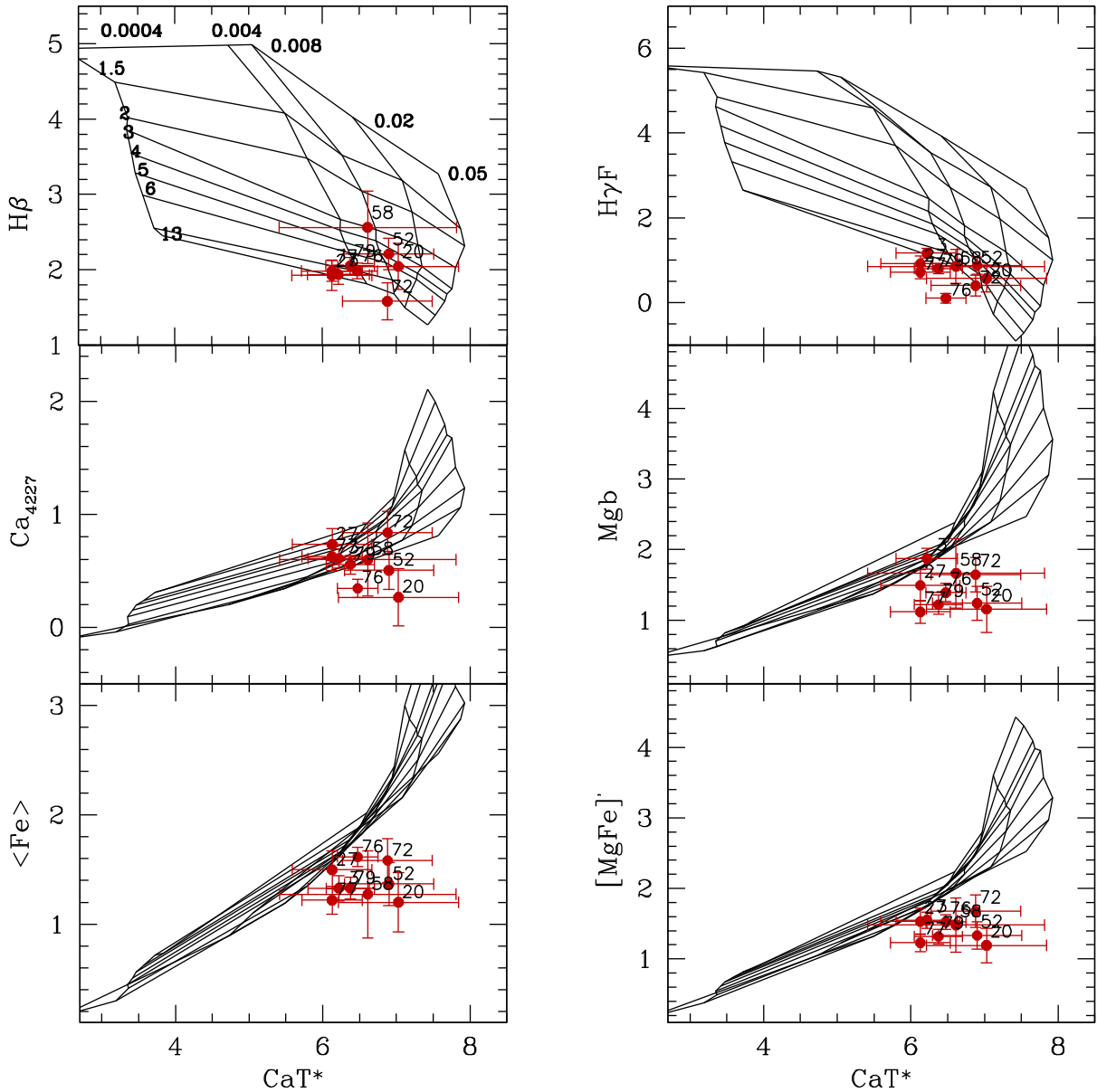


Figure 14. Cluster Lick indices versus the near-infrared CaT^* index. The data are for the NGC 4449 clusters, while the models are our ‘standard’ SSPs for $Z = 0.0004, 0.004, 0.008, 0.02, 0.05$, and ages from 1 to 13 Gyr. Notice that the ‘standard’ models are calibrated on Galactic stars and thus reflect the MW chemical composition ratios.

clusters preferentially located in the region of $[\alpha/\text{Fe}] < 0$. The same behaviour is observed in the Mgb versus $[\text{MgFe}]'$ plane. The Mgb index quantifies the strength of the $\text{Mg}b$ triplet at 5167, 5173, and 5184 Å, and is the most sensitive index to $[\alpha/\text{Fe}]$ variations among the Mg lines. Indeed, the Mg_1 and Mg_2 dependence on $[\alpha/\text{Fe}]$ is quite modest, in particular at low metallicities. The Mg_2 index is centred on the $\text{Mg}b$ feature, as the Mgb , while the Mg_1 samples MgH , FeI , and NiI lines at ~ 4930 Å. Both Mg_1 and Mg_2 pseudo-continua are defined on a ~ 400 Å baseline, much larger than the typical ~ 100 Å baseline of the other Lick indices, implying that Mg_1 and Mg_2 are potentially affected by uncertainties on the relative flux calibration. This could explain the mismatch observed between our cluster data and the models for both the indices: in fact, as discussed in Section 2, our observations were highly affected by differential flux losses due to atmospheric differential refraction and

it is possible that our correction, based on a few photometric bands, was not able to perfectly correct for this effect.

Finally, the $\text{H}\beta$, $\text{H}\gamma\text{A}$, and $\text{H}\gamma\text{F}$ versus $[\text{MgFe}]'$ planes provide the best separation between age and total metallicity. The $\text{H}\beta$ index is poorly affected by $[\alpha/\text{Fe}]$ variations, but suffers possible contamination from Balmer emission. On the other hand, the $\text{H}\gamma$ indices are less affected by emission than $\text{H}\beta$, but present a marked dependence on $[\alpha/\text{Fe}]$ due to the presence of several Fe lines in their pseudo-continua. We recall that our Balmer indices have been corrected for the presence of residual emission lines on the cluster spectra; the two only exceptions are clusters CL 39 and CL 8, not shown here, whose emission was too strong to attempt a recovery of the true absorption strengths. Cluster CL 24 was one of those with no visible emission lines in the final subtracted spectra; nevertheless, we notice that it falls slightly below the oldest models in all the

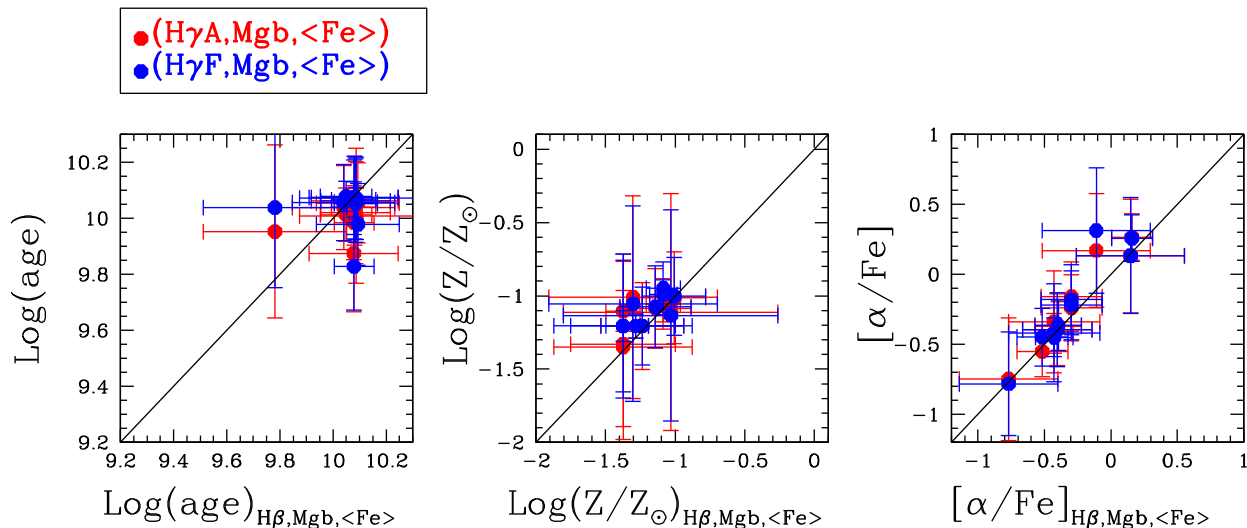


Figure 15. Ages, metallicities, and $[\alpha/\text{Fe}]$ ratios derived for clusters CL 20, CL 76, CL 72, CL 75, CL 79, CL 58, CL 52, CL 3, CL 77, CL 27, and CL 24 in NGC 4449 using different combinations of index triplets. The stellar population parameters obtained with the $(\text{H}\beta, \text{Mg}b, \langle \text{Fe} \rangle)$ triplet are on the x -axes, while the results from the other triplets, as indicated in the legend, are on the y -axes. The solid line is the one-to-one relation. Ages are in units of $\log_{10}(\text{age}[\text{yr}])$. The adopted solar metallicity is $Z_{\odot} = 0.018$.

$\text{H}\beta$, $\text{H}\gamma\text{A}$, $\text{H}\gamma\text{F}$ versus $[\text{MgFe}]'$ planes. All the other clusters fall within the model grid and are consistent with $Z \lesssim 0.004$ (or $Z \lesssim 0.008$, if we consider the models with $[\alpha/\text{Fe}] = -0.8$) and 4 Gyr \lesssim age \lesssim 13 Gyr. A more quantitative analysis of the stellar population parameters will be performed in the next section. Cluster CL 67, with Balmer indices as high as $\text{H}\beta = 6.4 \pm 0.6$, $\text{H}\gamma\text{A} = 10.1 \pm 0.7$, and $\text{H}\gamma\text{F} = 7.3 \pm 0.4$, falls outside the displayed index ranges, and it is a few hundred Myr old.

In Fig. 14, we plotted some key Lick indices versus the near-infrared CaT^* (Ca II triplet) index. We did not consider cluster CL 75 whose near-infrared spectrum was too noisy due to a non-optimal sky background subtraction. As previously noticed, no models with variable $[\alpha/\text{Fe}]$ ratios have been computed for the near-infrared indices and therefore the displayed SSPs refer to the base model⁵. Qualitatively, the CaT^* index provides results that are consistent with the Lick indices, with cluster total metallicities of $Z \lesssim 0.008$. The $\text{H}\beta$ versus CaT^* plane seems to be a viable alternative to the $\text{H}\beta$ versus $[\text{MgFe}]'$ diagram to disentangle age and metallicity effects. Although a discussion on the cluster element abundance ratios is not possible due to the lack of models different from the base one, we immediately notice the significant mismatch between data and models in the $\text{Mg}b$ versus CaT^* plane, confirming the low $[\alpha/\text{Fe}]$ ratios for our clusters.

4.2 Ages, metallicities, and $[\alpha/\text{Fe}]$ ratios

If we exclude the clusters with very strong emission contamination (i.e. clusters CL 39, CL 67, and CL 8) from our sample, we are left with a sub-sample of 11 clusters, namely CL 20, CL 76, CL 72, CL 75, CL 79, CL 58, CL 52, CL 3, CL 77, CL 27, and CL 24. For these clusters, we derived ages, metallicities, and $[\alpha/\text{Fe}]$ ratios using the algorithm described in Annibaldi et al. (2007). In brief, each SSP model of given age (t), metallicity (Z),

and $[\alpha/\text{Fe}]$ ratio (α) univocally corresponds to a point in a three-dimensional space defined by an index triplet. For each measured index triplet, we compute the *likelihood* that the generic (t, Z, α) model be the solution to that data point. This procedure provides a *likelihood* map in the three-dimensional (t, Z, α) space, and allows us to derive the ‘most probable’ solution with its associated uncertainty.

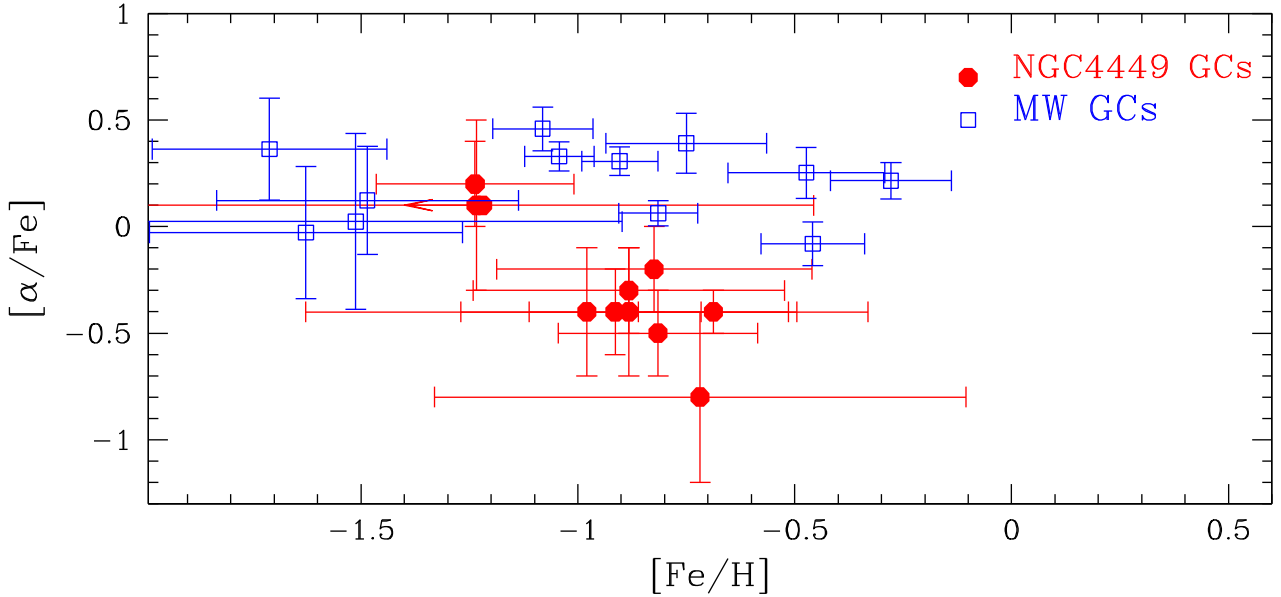
Following our discussion in Section 4.1, we selected in the first place the following indices for our stellar population study: $\text{H}\beta$, $\text{H}\gamma\text{A}$, $\text{H}\gamma\text{F}$, $\text{Mg}b$, $\text{Fe}5270$, and $\text{Fe}5335$. We then considered the following index triplet combinations, composed of an age-sensitive index and two metallicity-sensitive indices: $(\text{H}\beta, \text{Mg}b, \langle \text{Fe} \rangle)$, $(\text{H}\gamma\text{A}, \text{Mg}b, \langle \text{Fe} \rangle)$, $(\text{H}\gamma\text{F}, \text{Mg}b, \langle \text{Fe} \rangle)$, where $\langle \text{Fe} \rangle = 0.5 \times (\text{Fe}5270 + \text{Fe}5335)$. The CN_1 , CN_2 , and $\text{Ca}4227$ indices, potentially affected by CN variations, were analysed in a second step. For each triplet, we derived ages, total metallicities Z , and $[\alpha/\text{Fe}]$ ratios using our SSPs (Annibaldi et al. 2007, 2011a) and the algorithm described at the beginning of this section. The results are displayed in Fig. 15, where we plot the stellar population parameters obtained with the three different triplets. Fig. 15, left-hand panel, shows that the typical errors on the derived ages are quite large; the results obtained adopting different Balmer indices are highly scattered, although typically consistent with each other given the large errors on the ages. This large age uncertainty is the natural consequence of the progressively reduced age sensitivity of the Balmer absorption lines with increasing age: for instance, a $\sim 0.2 \text{ \AA}$ difference on the $\text{H}\beta$ index (which is the typical error for our clusters) corresponds to a several Gyr difference at old ages. On the other hand, the metallicity and the $[\alpha/\text{Fe}]$ values obtained with the different triplets are in quite good agreement, despite the age-metallicity degeneracy; this is due to the high capability of the Balmer + $\text{Mg}b$ + $\langle \text{Fe} \rangle$ diagnostic in separating age, metallicity, and α/Fe affects (e.g. Thomas et al. 2003).

In the end, we derived final ages, metallicities, and $[\alpha/\text{Fe}]$ ratios by averaging the results from the three different triplets, and computed the errors by propagating the uncertainties on the stellar population parameters. Table 6, where we summarize our results, shows that the majority of the analysed clusters are typically old

⁵ The base model uses FFs (Cenarro et al. 2002) calibrated on Galactic stars, and therefore reflects the MW chemical composition: $[\alpha/\text{Fe}] = 0$ at solar metallicities, and $[\alpha/\text{Fe}] > 0$ at sub-solar metallicities.

Table 6. Derived stellar population parameters for clusters in NGC 4449.

Cluster	Age (Gyr)	$\log(Z/Z_{\odot})$	$[\alpha/\text{Fe}]$	$[\text{Fe}/\text{H}]$	$[\text{N}/\alpha]$
CL 20	11 ± 5	-1.3 ± 0.5	-0.4 ± 0.3	-1.0 ± 0.6	< -0.5
CL 76	11 ± 2	-1.0 ± 0.1	-0.4 ± 0.1	-0.7 ± 0.2	-0.4 ± 0.2
CL 72	11 ± 4	-1.0 ± 0.3	-0.2 ± 0.2	-0.8 ± 0.4	> 0.5
CL 75	10 ± 4	-1.3 ± 0.5	-0.8 ± 0.4	-0.7 ± 0.6	> 0.5
CL 79	11 ± 2	-1.2 ± 0.1	-0.4 ± 0.2	-0.9 ± 0.2	-0.2 ± 0.2
CL 58	≥ 9	≤ -1.1	0.1 ± 0.4	≤ -1.2	0.5 ± 0.4
CL 52	11 ± 4	-1.2 ± 0.3	-0.4 ± 0.3	-0.9 ± 0.4	-0.1 ± 0.1
CL 3	9 ± 2	-1.0 ± 0.2	0.2 ± 0.2	-1.2 ± 0.2	-0.3 ± 0.2
CL 77	12 ± 2	-1.2 ± 0.1	-0.5 ± 0.2	-0.8 ± 0.2	< -0.5
CL 27	11 ± 4	-1.1 ± 0.3	-0.3 ± 0.2	-0.9 ± 0.3	-0.5 ± 0.2
CL 24	12 ± 4	-1.1 ± 0.6	0.1 ± 0.4	-1.2 ± 0.8	< -0.5

**Figure 16.** Distribution of clusters in NGC 4449 and in the MW in the $[\alpha/\text{Fe}]$ versus $[\text{Fe}/\text{H}]$ plane. The displayed MW clusters belong to the sample of Puzia et al. (2002) and are both halo and bulge GCs. The stellar population parameters of Galactic clusters have been obtained by reprocessing the Lick indices provided by Puzia et al. (2002) through our models for a self-consistent comparison with the NGC 4449 results.

(≥ 9 Gyr). The total metallicities are highly sub-solar, with $-1.3 \lesssim \log(Z/Z_{\odot}) \lesssim -1.0$; the majority of clusters have sub-solar $[\alpha/\text{Fe}]$ ratios (in the range -0.5 to -0.2), and only three clusters exhibit slightly super-solar $[\alpha/\text{Fe}]$ ratios. $[\text{Fe}/\text{H}]$ values were computed from the total metallicity Z and the $[\alpha/\text{Fe}]$ ratio through to the formula:

$$[\text{Fe}/\text{H}] = \log(Z/Z_{\odot}) + \log(f_{\text{Fe}}), \quad (3)$$

where we have assumed $Z_{\odot} = 0.018$, and f_{Fe} is the enhancement/depression factor of the Fe abundance in the models (see Annibali et al. 2007, for details).

NGC 4449's clusters are displayed in the $[\alpha/\text{Fe}]$ versus $[\text{Fe}/\text{H}]$ plane in Fig. 16, together with MW halo and bulge clusters from Puzia et al. (2002). For a self-consistent comparison, the Lick indices provided by Puzia et al. (2002) were reprocessed through our algorithm and models. The difference between clusters in NGC 4449 and in the MW is striking in this plane: while Galactic GCs exhibit a flat distribution with solar or super-solar $[\alpha/\text{Fe}]$ ratios at all metallicities, the clusters in NGC 4449 display a trend, with slightly super-solar $[\alpha/\text{Fe}]$ ratios at the lowest cluster metallicities,

and highly sub-solar $[\alpha/\text{Fe}]$ values at $[\text{Fe}/\text{H}] > -1$. Furthermore, the $[\text{Fe}/\text{H}]$ range of NGC 4449's clusters is between ~ -1.2 and -0.7 , higher than MW halo GCs and comparable to MW bulge clusters.

4.3 Nitrogen and carbon

The CN_1 , CN_2 , and $\text{Ca}4427$ indices, which are affected by CN abundance variations, can be used as diagnostics to study the nitrogen and carbon composition in our clusters. Fig. 11, left-hand panels, shows a remarkable difference in CN_1 , CN_2 , and $\text{Ca}4427$ between the bulk of clusters in NGC 4449 and Galactic GCs. In order to quantify this behaviour in terms of N and C abundance differences, we computed additional SSP models where we increased or depressed the abundance of C or N with respect to the solar-scaled composition. This resulted into models with different combinations of $([\alpha/\text{Fe}], [\text{N}/\alpha])$ or $([\alpha/\text{Fe}], [\text{C}/\alpha])$, shown in Fig. 17 together with the NGC 4449 and MW cluster data. The plotted models correspond to an age of 11 Gyr and $[\alpha/\text{Fe}] = -0.5$ to reflect the typical stellar population parameters derived for the NGC 4449's

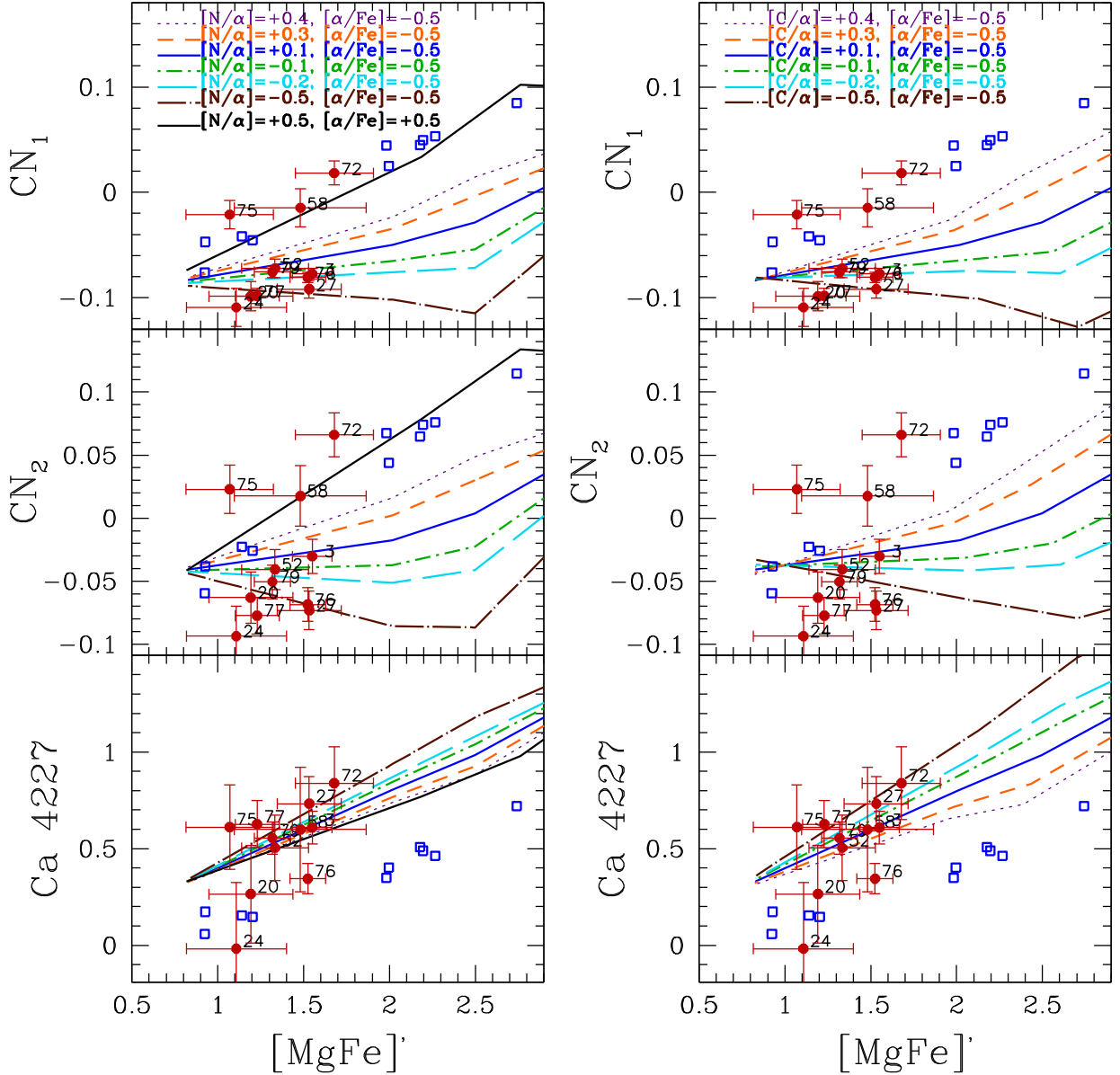


Figure 17. Distribution of NGC 4449's and MW clusters from Puzia et al. (2002, filled red circles and open blue squares, respectively) in the CN_1 , CN_2 , and $Ca4227$ versus $[MgFe]'$ planes. Overplotted are 11 Gyr old models for different combinations of $[\alpha/Fe]$ and $[N/\alpha]$.

clusters (see Table 6) and have $[N/\alpha]$ (or $[C/\alpha]$) values from -0.5 to $+0.5$. We also plotted an 11 Gyr model with $[\alpha/Fe] = +0.5$ and $[N/\alpha] = +0.5$ to account for the typical abundance ratios derived in Galactic GCs from integrated-light absorption features (e.g. Thomas et al. 2003). We notice that while the CN indices of Galactic GCs are well reproduced by N-enhanced models, the majority of clusters in NGC 4449, with the exception of clusters CL 72, CL 75, and CL 58 that are more compatible with the Galactic ones, require solar or sub-solar $[N/\alpha]$ (or $[C/\alpha]$) ratios to match the models. The $Ca4227$ index is less affected than CN_1 and CN_2 by CN abundance variations, and it is therefore less useful to characterize the chemical path of C and N. The $Ca4227$ indices measured by Puzia et al. (2002) for Galactic GCs are not well reproduced by the $[\alpha/Fe] = +0.5$, $[N/\alpha] = +0.5$ models and show an offset as large as $\sim -0.3 \text{ \AA}$.

The CN_1 , CN_2 , and $Ca4227$ indices alone do not allow us to break the degeneracy between C and N abundance variations. The

C_24668 and Mg_1 indices potentially offer a way out since they are much more sensitive to C than to N, but for our clusters they exhibit large errors or are not well calibrated, which makes them not very useful for our study. Thomas et al. (2003) showed that C-enhanced models could reproduce the large CN_1 and CN_2 indices observed in MW GCs, but failed in reproducing C_24668 and Mg_1 ; therefore, they concluded that a nitrogen rather than a carbon enhancement was more likely in Galactic GCs. Building on these results, we computed $[N/\alpha]$ values for the NGC 4449 clusters through comparison of the CN_1 and CN_2 indices against models where N is enhanced/depressed and C is left unchanged to the solar-scaled composition. We input into our algorithm, described in Section 4.2, the age, metallicity, and $[\alpha/Fe]$ values listed in Table 6, derived two different $[N/\alpha]$ ratios respectively from the $(CN_1, Mg_1, \langle Fe \rangle)$ and $(CN_2, Mg_1, \langle Fe \rangle)$ triplets, and then averaged the results. The mean $[N/\alpha]$ values, listed in column 6 of Table 6, are between -0.5 and -0.1 for all clusters but CL

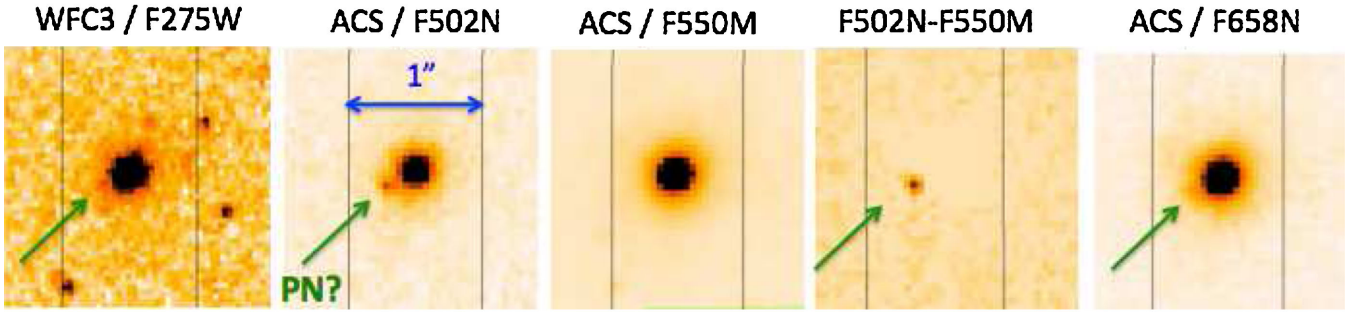


Figure 18. *HST* images of cluster CL 58 in different bands: *F275W* (NUV) from GO programme 13364 (PI: Calzetti), and *F502N* ([O III]), *F550M*, and *F658N* (H α) from GO programme 10522 (PI: Calzetti). The continuum-subtracted [O III] image (*F502N–F550M*) well shows the presence of a PN candidate in cluster CL 58. The PN is also detected in the NUV and (with a low signal-to-noise) in H α . Superimposed on the cluster is the 1-arcsec-wide slit used in our MODS observation.

72, CL 75, and CL 58, which exhibit highly super-solar $[N/\alpha]$ ratios.

5 A PN WITHIN CLUSTER CL 58?

As discussed in Section 2, the emission lines observed in the MODS spectrum of cluster CL 58 are not due to the extended ionized gas present in NGC 4449, but instead appear to originate within the cluster itself. In order to investigate the origin of this centrally concentrated emission, we inspected *HST* images in different bands, with a spatial resolution ~ 10 times better than the typical seeing of our observations. In particular, we show in Fig. 18 images of cluster CL 58 in *F275W* (NUV) from GO programme 13364 (PI: Calzetti), and in *F502N* ([O III]), *F550M* (continuum near [O III]), and in *F658N* (H α) from GO programme 10522 (PI: Calzetti). These images, and in particular the continuum-subtracted [O III] image (*F502N–F550M*), reveal the presence of a source with strong emission in [O III] at a projected distance of ~ 0.25 arcsec from the cluster centre; this source is also visible in the NUV image and in H α (with a lower contrast than in [O III]), while it is not visible in the *F550M* continuum image. All these properties suggest that it may be a PN belonging to the cluster, although we cannot exclude a chance superposition of a ‘field’ PN at the cluster position. The [O III] emission inferred from our MODS spectrum of CL 58 is $\sim 3 \times 10^{-16}$ erg s $^{-1}$ cm $^{-2}$ (see Table 5), compatible with the brightest PNe detected in NGC 4449 (Annibali et al. 2017).

PNe in GCs are rare. Only four PNe are known in Galactic GCs so far (Pease 1928; Gillett et al. 1989; Jacoby et al. 1997). Jacoby et al. (2013) identified 3 PN candidates in a sample of 274 M31 GCs. Bond (2015) analysed *HST* data of 75 extragalactic GCs in different Local Group galaxies (LMC, M31, M33, NGC 147, NGC 6822) to search for PNe, and found only two (doubtful) candidates in the vicinity of the M31 GC B086. A PN was discovered in the NGC 5128 (CenA) GC G169 by Minniti & Rejkuba (2002), and one in the Fornax GC H5 by Larsen (2008). We visually inspected the continuum-subtracted [O III] image of NGC 4449 to search for additional PN candidates associated with ‘old’ (> 1 Gyr, from integrated colours) clusters in the *All* catalogue (only 20 of them fall within the *F502N* field of view), but could not find any. Therefore, we are left with one PN detection out of a sample of 20 old clusters in NGC 4449. To our knowledge, CL 58 is the only known dwarf irregular (dIrr) GC to host a candidate PN.

According to stellar evolution, GCs as old as the Galactic ones should be unable to host PNe, because in such old populations the masses of stars that are today transiting between the asymptotic

giant branch (AGB) and the white dwarf phase are smaller than $\sim 0.55 M_{\odot}$ (see Jacoby et al. 2017, and references therein). Some sort of binary interaction has therefore been suggested to explain the presence of the (few) PNe detected in old Galactic GCs (Jacoby et al. 1997). On the other hand, GCs with intermediate rather than extremely old ages are expected to be richer in PNe than MW GCs. For the NGC 4449 GCs, ages are derived with very large uncertainties; nevertheless, as we will discuss in Section 7, the derived chemical paths tend to exclude a rapid and early cluster formation as in the case of the MW. The idea that NGC 4449 lacks or has very few, old clusters is reinforced by our detection of one PN out of 20 analysed clusters, a frequency higher than that derived in the MW or in M31.

6 DYNAMICAL PROPERTIES OF NGC 4449

We can use the cluster velocities to probe the properties of the cluster population, and of NGC 4449 as a whole.

6.1 Systemic velocity and cluster velocity dispersion

Using the central coordinates and distance of NGC 4449 given in Section 1, along with the cluster coordinates in Table 3, we calculate the projected distance of each cluster from the centre of NGC 4449. The farthest cluster in our sample lies at a projected distance $R_{\max} = 2.88$ kpc from the centre of NGC 4449.

We augment our data with the cluster sample from Strader et al. (2012), removing any duplicates. This provides an additional 23 clusters. These clusters come partly from the same field as our sample, with some additional clusters detected in the Sloan Digital Sky Survey (SDSS) data. There are very few clusters outside the range of our field, and the sample is likely to be incomplete. As such, we elect to include only the seven additional clusters inside R_{\max} ; this leaves us with a sample of 19 clusters in total. Another reason for this choice is that, in the next section, we will use the cluster velocities to estimate the mass of NGC 4449; including the clusters outside R_{\max} could significantly bias our mass estimates as they would hinge on just one or two distant clusters.

We use a simple maximum-likelihood estimator to evaluate the mean velocity $v = 203 \pm 11$ km s $^{-1}$ and velocity dispersion $\sigma = 45 \pm 8$ km s $^{-1}$ of the cluster sample. We will adopt the mean as the systemic velocity of NGC 4449 and subtract it from the individual cluster velocities in subsequent analysis. The systemic velocity is in good agreement with the systemic velocity estimate of 205 ± 1 km s $^{-1}$ from Hunter et al. (2005) and of 204 ± 2 km s $^{-1}$

from Strader et al. (2012), though smaller than earlier estimates of $\sim 214 \text{ km s}^{-1}$ from Bajaja, Huchtmeier & Klein (1994) and Hunter et al. (2002).

Velocity measurements of H I gas find that the velocity dispersion of NGC 4449 varies from 15 to 35 km s^{-1} through the galaxy (Hunter et al. 2005), slightly lower than we find here for the central GC population. H α measurements find even higher dispersions, with a global average dispersion of $31.5 \pm 10 \text{ km s}^{-1}$ measured by Valdez-Gutiérrez et al. (2002), though they note that the dispersion increases to $\sim 40 \text{ km s}^{-1}$ in the bar region near the centre, in good agreement with our cluster measurement. These dispersions are generally higher than would be expected, which is indicative of a system that is highly perturbed due to intense SF (Hunter et al. 1998).

6.2 Dynamical mass estimate

We can also use the radial velocities along with the positions of the clusters to estimate the total mass of NGC 4449 within the region spanned by the clusters, that is inside R_{max} . To do this, we use the tracer mass estimators introduced in Watkins, Evans & An (2010), which are simple and yet remarkably effective. There are a number of estimators depending on the type of distances and velocities available; given the data we have, we use the estimator requiring projected distances and line-of-sight velocities here.

The tracer mass estimators assume that, over the region of interest, the tracer sample has a number density distribution that is a power law with index $-\gamma$, has a potential that is a power law with index $-\alpha$, and has a constant anisotropy β . We assume that the sample is isotropic and thus that $\beta = 0$. The other two parameters require further consideration.

To estimate the power-law index γ for the number density distribution, we combined the GC samples from *A11* and Strader et al. (2012). As we are only concerned with the number density distribution here, we can use all clusters, regardless of whether or not they also have velocity measurements. With duplicates removed, this leaves a sample of 157 clusters. Again using the central coordinates and distance of NGC 4449, we calculate the projected distance of each cluster from the centre and then calculate the projected cumulative number profile. To estimate γ , we fit to this cumulative profile only in the region where we have velocity data ($0.17 < R < 2.88 \text{ kpc}$) assuming an underlying power-law density and obtain a best-fitting power-law index $\gamma = 2.18 \pm 0.01$, where the uncertainty indicates the uncertainty in the fit for the particular model we have assumed and does not account for any additional uncertainties.

To get a better estimate of the uncertainty in γ , we also fit a double power law, where we assume that the power-law index is γ_{in} for $R \leq R_{\text{break}}$ and is γ_{out} for $R > R_{\text{break}}$ for some break radius R_{break} , to the full cluster position sample. The best fit gives $\gamma_{\text{in}} = 1.78 \pm 0.01$ and $\gamma_{\text{out}} = 4.41 \pm 0.03$ with $R_{\text{break}} = 1.59 \pm 0.01 \text{ kpc}$. So we will use $\gamma = 2.18$ to obtain our best mass estimate, but use the range $1.78 \leq \gamma \leq 4.41$ to provide uncertainties on the mass estimate.

Fig. 19 shows the results of these fits. The black line shows the cumulative number density profile of the data, the orange line shows the best-fitting single power law in the region of interest (the boundaries of which are marked by the vertical dotted lines), the solid blue line shows the best-fitting double power law to the whole sample, and the dashed blue line marks the break radius for the double power-law fit. The best-fitting power-law indices for the fits are also given.

To estimate the power-law index α of the potential, we assume that NGC 4449 has a baryonic component embedded in a large dark

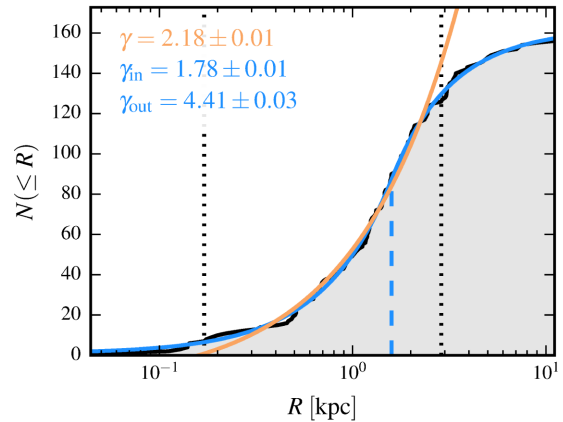


Figure 19. The cumulative number density profile of GCs in NGC 4449. The black line shows the profile measured from the combined catalogues of *A11* and Strader et al. (2012). The orange line shows the best-fitting profile to the region of interest (marked by vertical dotted lines) assuming that the underlying density profile is a power law. The index of the power law γ is given in orange in the top-left corner. The blue line shows the best-fitting profile to the whole sample assuming that the underlying density profile is a double power law with an inner index of γ_{in} and an outer index γ_{out} (shown in blue in the top-left corner). The radius at which the power-law index changes from inner to outer is marked by the blue vertical dashed line. We use the single fit as the best estimate of the power law in this region and use the indices from the double fit to provide uncertainties.

matter (DM) halo. The power-law slope of the potential will depend on which of these components dominates inside R_{max} , or indeed, if both make significant contributions to the potential. If the baryonic component is dominant so that mass follows light, then $\alpha = \gamma - 2$ for $\gamma \leq 3$ and $\alpha = 1$ for $\gamma > 3$. For the range of γ we found above, this would imply a range of $-0.22 \leq \alpha \leq 1$ with a best estimate of $\alpha = 0.18$.

To estimate α for the case where the DM component is dominant, we assume that the DM halo of NGC 4449 is Navarro, Frenk & White (1997, hereafter NFW), but with unknown virial radius and concentration. However, although we do not know the exact halo parameters, we can still place some constraints on these values. The virial radius is likely to be smaller than the MW’s value of $r_{\text{vir}} \sim 258 \text{ kpc}$, and the concentration is likely to be between the MW’s value of $c \sim 12$ and the typical concentration of dSphs $c \sim 20$. Guided by these constraints, we try a grid of virial radii ($80 \leq r_{\text{vir}} \leq 200 \text{ kpc}$) and concentrations ($10 \leq c \leq 20$) and find the power law that best fits the slope of the potential in the region of interest for each halo.

To further narrow down the choice of likely haloes, we turn to H I measurements, which find a rotation speed, corrected for inclination, of 84 km s^{-1} at 15.7 kpc (Bajaja et al. 1994; Martin 1998). If we insist that the circular velocity at 15.7 kpc must be within 10 km s^{-1} of the H α measurements, then this restricts the virial radius and concentration combinations allowed. Fig. 20 shows how α varies over the halo grid for the ‘allowed’ haloes only. These remaining haloes follow a curve in the $r_{\text{virial}}-c$ plane, and predict $0.05 \lesssim \alpha \lesssim 0.13$ with a mean $\alpha \sim 0.09$, which, we note, is much narrower than the mass-follows-light case.

However, we must still consider whether the DM is the dominant mass component inside R_{max} or if the baryonic mass dominates the form of the potential. Using $\gamma = 2.18$ as previously determined, the total mass enclosed within R_{max} for this range of α values shows little variation (only ~ 1 per cent). However, the total DM mass

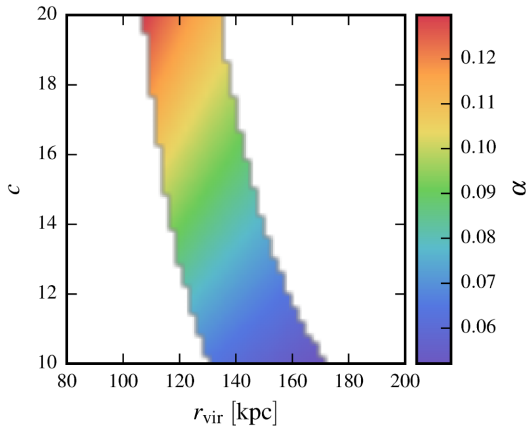


Figure 20. The variation in potential slope α for a grid of DM haloes assumed to be NFW in shape and defined by a concentration c and a virial radius r_{vir} . To each halo, we fit a power law over the range of interest for our mass estimation – the colour bar shows how the index α of the best-fitting power law changes from halo to halo. We only show haloes with circular velocities at 15.7 kpc of $84 \pm 10 \text{ km s}^{-1}$ to force consistency with H I observations. The white regions are haloes with circular velocities outside this range.

inside R_{max} changes significantly from halo to halo, such that the DM is approximately half of the total mass at its lowest and apparently exceeds the total mass at its highest (we choose not to rule out these haloes as a larger γ would alleviate this problem). Overall, we conclude that the DM makes a significant or dominant contribution to the mass within R_{max} and so it would be incorrect to assume that mass follows light. So we will use the mean value of $\alpha = 0.09$ found from the NFW fitting to obtain our best mass estimate, but, to be conservative, use the broader range $-0.22 \leq \gamma \leq 1$ to provide uncertainties on the mass estimate.

Now that we have estimates for α and γ , we can proceed with the mass estimates. As discussed, we will use our best estimates of $\alpha = 0.09$ and $\gamma = 2.18$, to get a ‘best’ mass estimate; and to estimate the uncertainty in the mass, we will calculate the mass estimate across $-0.22 \leq \alpha \leq 1$ and $1.78 \leq \gamma \leq 4.41$. Fig. 21 shows the results of these calculations. For each α - γ combination across the grid, we estimate the mass inside R_{max} . The solid black lines show our adopted ‘best’ α and γ values. The dotted black lines show the range of α predicted from the NFW halo fitting. The white line traces the results if we were to assume that mass follows light. We see that the mass estimate is dominated by the assumed value of γ and is much less sensitive to the value of α . Overall, we estimate the mass of NGC 4449 inside 2.88 kpc to be $M(< 2.88 \text{ kpc}) = 3.15^{+3.16}_{-0.75} \times 10^9 M_{\odot}$. The implied circular velocity at $R_{\text{max}} = 2.88 \text{ kpc}$ is $69^{+29}_{-9} \text{ km s}^{-1}$. By comparison, Martin (1998) estimated a rotation of $\sim 40 \text{ km s}^{-1}$ at $\sim 3 \text{ kpc}$ using H I observations, which is somewhat lower than our estimate here. However, the significant velocity dispersion of the H I (see Section 6.1) implies that the H I rotation speed should indeed be below the circular velocity to maintain hydrostatic equilibrium.

Hunter et al. (2002) found a minimum in the H I distribution at the centre of NGC 4449, and estimated that the H I mass inside 2 arcmin ($\sim 2.2 \text{ kpc}$) is just $3 \times 10^8 M_{\odot}$. Assuming that the mass increases linearly with radius, the H I mass inside R_{max} would be $\sim 4 \times 10^8 M_{\odot}$, so the H I makes up a little more than 10 per cent of the total mass near the centre. The total mass was estimated from H I observations to be $\sim 7.8 \times 10^{10} M_{\odot}$ inside 30 arcmin ($\sim 33 \text{ kpc}$). If we assume that NGC 4449 has a flat rotation curve, and thus that

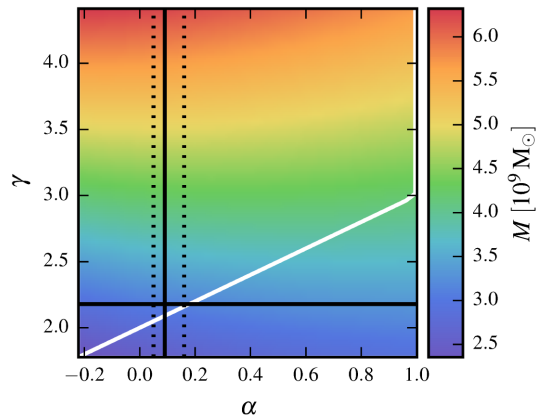


Figure 21. The variation in estimated mass inside 2.88 kpc as a function of potential slope α and density slope γ . The range of γ was set by fitting to existing GC data. The range of α was set by assuming that mass follows light, in which case $\alpha = \min(1, \gamma - 2)$ (marked by the white line), as this range was larger than that estimated from considering DM halo models (highlighted by vertical dotted lines). The solid black lines show our best estimates for α and γ , and their intersection shows the adopted best mass estimate. The minimum and maximum masses in this grid set our uncertainties.

the mass increases linearly with radius, our mass estimate would imply a total mass $\sim 3.6^{+3.6}_{-0.9} \times 10^{10} M_{\odot}$ within 30 arcmin, which is inconsistent with the H I measurements, even given our rather generous upper mass limit. Furthermore, our estimate is likely to be an overestimate as the assumption of a flat rotation curve is likely reasonable near the centre but may break down towards larger radii, thus creating more tension with the mass implied by H I data.

NGC 4449 is often considered an analogue of the LMC. By comparison, van der Marel & Kallivayalil (2014) find a mass $M(< 8.7 \text{ kpc}) = 17 \pm 7 \times 10^9 M_{\odot}$ for the LMC. Again assuming that the mass increases linearly with radius, then our mass measurement would imply a mass of $\sim 9.5 \times 10^9 M_{\odot}$ at 8.7 kpc, with the uncertainties encompassing 7 – $19 \times 10^9 M_{\odot}$. This estimate is lower than the LMC estimate, but still consistent at the upper end of the uncertainty range.

7 DISCUSSION

From our stellar population study of old clusters in NGC 4449, we find that the large majority of them have solar or sub-solar $[\alpha/\text{Fe}]$ and $[\text{N}/\alpha]$ ratios, making them clearly different with respect to Galactic GCs. These chemical properties have strong implications on our understanding of the formation of GCs in this irregular galaxy, which we discuss in the following.

7.1 $[\alpha/\text{Fe}]$ ratios

It is well known that the $[\alpha/\text{Fe}]$ ratio quantifies the relative importance of high-mass stars versus intermediate-/low-mass stars to the enrichment of the interstellar medium (ISM), and it is therefore tightly linked to both the stellar initial mass function (IMF) and to the SF time-scale (e.g. Greggio & Renzini 1983; Tornambe & Matteucci 1986). In fact, α -elements (O, Ne, Mg, Si, S, Ar, Ca, Ti) are mainly synthesized by massive stars and restored into the ISM on short SF time-scales ($\lesssim 50 \text{ Myr}$), while Fe, mostly provided by SNIa, is injected into the ISM on longer time-scales. Soon as SNIa start to contribute, they dominate the iron enrichment and $[\alpha/\text{Fe}]$ inevitably decreases: Matteucci & Recchi (2001) estimated that the

time in maximum enrichment by SNIa varies from ~ 40 – 50 Myr for an instantaneous starburst to ~ 0.3 Gyr for a typical elliptical galaxy to ~ 4 – 5 Gyr for a spiral galaxy. Therefore, under the assumption of a universal IMF, super-solar $[\alpha/\text{Fe}]$ ratios can be interpreted as the signature of an early and rapid SF (e.g. in giant elliptical galaxies, or in the halo’s field stars and GCs of spiral galaxies), while sub-solar $[\alpha/\text{Fe}]$ indicate a prolonged SF, more typical of dwarf systems (e.g. Matteucci & Tosi 1985; Lanfranchi & Matteucci 2003). In dwarf galaxies, galactic winds powered by massive stars and SNII explosions may also play an important role in lowering the $[\alpha/\text{Fe}]$ value through expulsion of the newly produced α -elements: Marconi, Matteucci & Tosi (1994) showed that sub-solar $[\alpha/\text{Fe}]$ ratios can be obtained in dwarf galaxies by assuming differential galactic winds that are more efficient in removing the α -elements than Fe since activated only during the bursts where most of the α -elements are formed. Alternatively, different $[\alpha/\text{Fe}]$ ratios could be due to a non-universal IMF: for instance, it has been suggested that the IMF could have been skewed towards massive stars in elliptical galaxies and in the bulge, producing the observed super-solar α/Fe ratios, and towards low-mass stars in dwarf galaxies (e.g. Weidner et al. 2013; Yan, Jerabkova & Kroupa 2017).

From an observational point of view, chemical abundances of individual RGB stars have been extensively derived in the nearest dSphs (e.g. Shetrone, Bolte & Stetson 1998; Shetrone, Côté & Sargent 2001; Tolstoy et al. 2003; Kirby et al. 2011; Lemasle et al. 2014; Hasselquist et al. 2017; Norris et al. 2017). These studies have shown that each dSph starts, at low $[\text{Fe}/\text{H}]$, with super-solar $[\alpha/\text{Fe}]$ ratios, similar to those in the MW halo at low metallicities, and then the $[\alpha/\text{Fe}]$ ratio evolves down to lower values than are seen in the MW at high metallicities (see Tolstoy, Hill & Tosi 2009, for a review). The ‘knee’, i.e. the position where $[\alpha/\text{Fe}]$ starts to decrease, depends on the particular SFH of the galaxy and occurs at larger $[\text{Fe}/\text{H}]$ for a more rapid SF and a more efficient chemical enrichment. The general finding in dSphs that relatively metal rich ($[\text{Fe}/\text{H}] > -1$) stars are deficient in α -elements compared to iron suggests that the most recent generations of stars were formed from an ISM relatively poor in the ejecta from SNII.

The observational picture is far less complete for dIrr galaxies because of their larger distance from the MW compared to dSphs (with the obvious exceptions of the LMC and the SMC). Chemical abundance determinations in these systems are mainly limited to H II regions (e.g. Izotov & Thuan 1999; Kniazev et al. 2005; Magrini et al. 2005; van Zee & Haynes 2006; Guseva et al. 2011; Berg et al. 2012; Haurberg, Rosenberg & Salzer 2013) and to a few supergiant stars (Venn et al. 2001, 2003; Kaufer et al. 2004; Leaman et al. 2009, 2013), which probe a look-back time of at most ~ 10 Myr. Chemical abundance studies of PNe (e.g. Magrini et al. 2005; Peña, Stasińska, Richer 2007; García-Rojas et al. 2016; Annibali et al. 2017; Flores-Durán, Peña, Ruiz 2017) and unresolved star clusters (e.g. Strader et al. 2003; Puzia & Sharina 2008; Sharina et al. 2010; Hwang et al. 2014) provide a valuable tool to explore more ancient epochs and have been attempted in a few dIrrs. The H II region and young supergiant tracers indicate typically low $[\alpha/\text{Fe}]$ ratios, as expected in galaxies that have formed stars at a low rate over a long period of time and where galactic winds may have possibly contributed to the expulsion of the α -elements. Interestingly, also integrated-light studies of GCs in dIrrs provide solar or slightly sub-solar $[\alpha/\text{Fe}]$ values, in agreement with our results. In NGC 4449, we find only a minority of clusters (three in our sample) with super-solar $[\alpha/\text{Fe}]$ ratios at $[\text{Fe}/\text{H}] \lesssim -1.2$, while the majority of clusters (eight in our sample) display intermediate metallicities ($-1 \lesssim [\text{Fe}/\text{H}] \lesssim -0.5$) and sub-solar $[\alpha/\text{Fe}]$ values. This indicates that the NGC 4449’s

clusters have typically formed from a medium already enriched in the products of SNIa and relatively poor, compared to the solar neighbourhood, in the products of massive stars and SNII (either because of the slower SFH and/or because of preferential loss of α -elements due to galactic winds). From our data, there are hints that the *knee* occurs at $[\text{Fe}/\text{H}] \leq -1.2$ to -1.0 , although a larger cluster sample would be needed to reinforce this result. In particular, we do not observe a very metal poor (i.e. $[\text{Fe}/\text{H}] < -1.5$), α -enhanced cluster population in our sample. Whether such a population is present at larger galactocentric distances than those sampled by our data [e.g. Strader et al. (2012) identified possible cluster candidates in the outer halo of NGC 4449], or if such a component is absent due to the lack of a major SF event at early times in NGC 4449, cannot be established from our data. Indeed, resolved star CMDs indicate a low activity at ancient epochs in dIrrs as opposed to an early peak in the SFH of dSphs (e.g. Monelli et al. 2010; Weisz et al. 2014; Skillman et al. 2017); this behaviour could naturally explain the different chemical paths observed in dSphs and dIrrs. The idea that the typical GC population in NGC 4449 is younger than in the MW is reinforced by our serendipitous detection of a PN in cluster CL 58 (see Section 5).

A useful comparison is that between NGC 4449 and the LMC, the irregular whose star cluster system is the best studied. The LMC GCs span a wide age/metallicity range, with both old, metal-poor and young, metal-rich objects, due to its complex SFH. Chemical abundances of individual RGB stars in LMC clusters have been derived by several authors (e.g. Hill et al. 2000; Johnson, Ivans & Stetson 2006; Mucciarelli, Origlia & Ferraro 2010). These studies show that old LMC clusters display a behaviour of $[\alpha/\text{Fe}]$ as a function of $[\text{Fe}/\text{H}]$ similar to the one observed in the MW stars, with old LMC clusters having $[\alpha/\text{Fe}] \sim 0.3$; these clusters should therefore have formed during a rapid SF event that occurred at early times, when the ISM was not yet significantly enriched by the products of SNIa. However, the majority of clusters in the LMC exhibit relatively ‘young’ ages and intermediate metallicities 1–3 Gyr, $[\text{Fe}/\text{H}] \sim -0.5$ coupled with low $[\alpha/\text{Fe}]$ values, more chemically similar to the clusters in NGC 4449. A possible explanation is that the LMC has formed the majority of its GCs from a medium already enriched by SNIa.

Two of the most luminous clusters in our sample, namely clusters CL 77 and CL 79, were also studied by Strader et al. (2012) through spectroscopy (their clusters B15 and B13, respectively). These clusters appear peculiar in that they are quite massive ($M_* \sim 2 \times 10^6 M_\odot$, comparable to the mass of ωCen in the MW, that is thought to be the remnant nucleus of an accreted dwarf galaxy) and elongated ($1 - b/a \sim 0.2$ – 0.3); cluster CL 77 is furthermore associated in projection with two tails of blue stars whose shape is reminiscent of tidal tails, and has therefore been suggested to be the nucleus of a former gas-rich satellite galaxy undergoing tidal disruption by NGC 4449 (Annibali et al. 2012). For clusters CL 77 and CL 79, Strader et al. (2012) derived ages of 11.6 ± 1.8 and 7.1 ± 0.5 Gyr, a common metallicity of $[\text{Fe}/\text{H}] = -1.12 \pm 0.06$ dex, and $[\alpha/\text{Fe}]$ values of -0.2 ± 0.1 and -0.1 ± 0.1 , respectively; these results are marginally consistent with our age estimates of 12 ± 2 and 11 ± 2 Gyr, $[\text{Fe}/\text{H}]$ metallicities of -0.8 ± 0.2 and -0.9 ± 0.2 dex, and $[\alpha/\text{Fe}]$ ratios of -0.5 ± 0.2 and -0.4 ± 0.2 , respectively. While the relatively poor signal-to-noise of the Strader et al. (2012) spectra did not allow them to derive the stellar population parameters for other clusters in NGC 4449 than CL 77 and CL 79, our study shows that the presence of sub-solar $[\alpha/\text{Fe}]$ values is a typical characteristic of the NGC 4449’s clusters and not just a peculiarity of clusters CL 77 and CL 79.

7.2 [N/α] ratios

Besides displaying sub-solar $[\alpha/\text{Fe}]$, the majority of clusters in NGC 4449 appear peculiar also in their CN content, as quantified by the CN_1 and CN_2 indices: compared to Galactic GCs (or to M31 GCs), they show lower CN indices at the same metallicities. The CN absorption strength is sensitive to the abundances of both carbon and nitrogen; however, the CN lines observed in Galactic GCs are well reproduced by models in which N, rather than C, is enhanced with respect to the solar composition (e.g. Thomas, Maraston & Bender 2003; Puzia, Perrett & Bridges 2005): the reason is that a C enhancement would result also into a significant increment of the C_24668 and Mg_1 indices, in disagreement with the observations. Using Lick indices, Thomas et al. (2003) derived $[\text{N}/\alpha] \sim 0.5$ for Galactic GCs.

Recent progress in studies of GCs has shown that they contain multiple stellar populations (e.g. Piotto et al. 2015): at least two populations of stars are present, one with the same chemical pattern as halo-field stars, and second ones that are enhanced in helium, nitrogen, and sodium and depleted in carbon and oxygen (e.g. Gratton, Carretta & Bragaglia 2012). A possible scenario to explain this multiplicity is that the second populations have formed from a material enriched from the ejecta of intermediate-mass AGB stars (e.g. Renzini et al. 2015; D’Antona et al. 2016). While the presence of multiple populations seems so far to be ubiquitous in GCs, the fraction of first- over second-generation stars varies from cluster to cluster, with the first generation of stars typically being the minority; therefore, we would expect the second, N-enriched generations of stars to dominate the integrated cluster light and to drive the large N-enrichment observed in the integrated spectra of Galactic GCs. The scenarios to interpret the cluster multiple populations are still very uncertain though, and none of them provide a good explanation for all their observed properties yet (Bastian & Lardo 2017).

With the exception of CL 72, CL 75, and CL 58, the CN_1 and CN_2 indices for the clusters in NGC 4449 lie slightly below the models with $[\text{N}/\alpha]$, $[\text{C}/\alpha] = 0$. Unfortunately, our data do not allow us to establish if the low CN absorption is due to either an N or to a C depletion: in fact, as already discussed in Section 4.3, the C_24668 and Mg_1 indices, which are highly sensitive to C and could in principle allow for a discrimination between the two effects, show a very large scatter in our sample and are not well calibrated. Under the assumption that the low observed CN strength is due to an N depletion, we computed N/α ratios for the clusters and found $-0.5 \lesssim [\text{N}/\alpha] \lesssim -0.1$ (while clusters CL 72, CL 75, and CL 58 show highly super-solar ratios of $[\text{N}/\alpha] > 0.5$). We stress that, although our data do not permit discrimination between N and C depletion, we can definitively exclude for the majority of clusters in NGC 4449 the presence of a major N-enriched component similar to that observed for old Galactic GCs. However, we cannot exclude the presence of intrinsic light-element variations, although to a different extent with respect to MW GCs (see e.g. the case of cluster NGC 419 in the SMC; Martocchia et al. 2017).

7.3 Comparison between gas and star metallicities

From our spectroscopic study, we derived cluster total metallicities in the range $-1.3 \lesssim \log Z/Z_\odot \lesssim -1.0$ (see Table 6), for an adopted solar metallicity of $Z_\odot = 0.018$. Since the total metal fraction is mainly driven by oxygen, it is sensible to compare these values with oxygen abundance determinations in NGC 4449’s H II regions, which trace the present-day ISM composition. Berg et al. (2012) and Annibali et al. (2017) derived metallicities in the range

$8.26 \lesssim 12 + \log (\text{O}/\text{H}) \lesssim 8.37$; this translates, for an assumed solar oxygen abundance of $12 + \log (\text{O}/\text{H})_\odot = 8.83 \pm 0.06$ (Grevesse & Sauval 1998)⁶, into $-0.57 \lesssim \log ((\text{O}/\text{H})/(\text{O}/\text{H})_\odot) \lesssim -0.46$. This result indicates a $\gtrsim 0.5$ dex metal enrichment in NGC 4449 within the last ~ 10 Gyr, which is the typical age of the clusters in our sample. A spectroscopic estimate of NGC 4449’s stellar metallicity was also derived by Karczewski et al. (2013): they inferred an average $\sim 1/5$ solar metallicity for the stellar population older than 1 Gyr, which is ‘qualitatively’ consistent with the $\sim 1/10$ solar metallicity derived in this paper for our ~ 10 Gyr old stellar clusters. In a future paper (Romano et al., in preparation), we will use all the available information on the chemical properties of the stellar and gaseous components in NGC 4449 to run chemical evolution models that will allow us to produce a self-consistent scenario for the evolution of this galaxy.

8 CONCLUSIONS

We acquired intermediate-resolution ($R \sim 1000$) spectra in the range $\sim 3500\text{--}10\,000$ Å with the MODS instrument on the LBT for a sample of 14 star clusters in the irregular galaxy NGC 4449. The clusters were selected from the sample of 81 young and old clusters of A11. With the purpose of studying the integrated-light stellar population properties, we derived for our clusters Lick indices in the optical and the Ca II triplet index in the near-infrared. The indices were then compared with SSP models to derive ages, metallicities, $[\alpha/\text{Fe}]$ and $[\text{N}/\alpha]$ ratios. Of the 14 clusters observed with MODS, three are affected by a major contamination from the diffuse ionized gas in NGC 4449 (in particular, one of these is a \sim few hundred Myr old cluster). Therefore, we are left with a sub-sample of 11 clusters for which we could perform a reliable stellar population analysis. For this sub-sample, the main results are as follows.

(i) The clusters have intermediate metallicities, in the range $-1.2 \lesssim [\text{Fe}/\text{H}] \lesssim -0.7$; the ages are typically older than ~ 9 Gyr, although determined with large uncertainties. No cluster with iron metallicity as low ($-2 \lesssim [\text{Fe}/\text{H}] \lesssim -1.2$) as in MW GCs is found in our sample.

(ii) The majority of clusters exhibit sub-solar α/Fe ratios (with a peak at $[\alpha/\text{Fe}] \sim -0.4$), suggesting that they formed from a medium already enriched in the products of SNIa. Sub-solar $[\alpha/\text{Fe}]$ values are expected in galaxies that formed stars inefficiently and at a low rate and/or where galactic winds possibly contributed to the expulsion of the α -elements.

(iii) Besides the low $[\alpha/\text{Fe}]$, the majority of clusters in NGC 4449 appear also to be underabundant in CN compared to MW halo GCs. A possible explanation is the lack of a major contribution from N-enriched, second-generation stars as those detected in the old, metal-poor galactic GCs. Intrinsic light-element variations may still be present within NGC 4449’s GCs, but to a different extent with respect to MW clusters.

(iv) We report the serendipitous detection of a PN within cluster CL 58 out of a sample of 20 ‘old’ (> 1 Gyr, from integrated colours) clusters in NGC 4449 covered by ACS/F502N and ACS/F555M images. PNe in old MW and M31 GCs are extremely rare, and our result reinforces the idea that the cluster population in NGC 4449 is typically younger than in these two giant spirals.

⁶ We adopt $12 + \log (\text{O}/\text{H})_\odot = 8.83 \pm 0.06$ and $Z_\odot = 0.018$ instead of the lower, more recent estimates of $12 + \log (\text{O}/\text{H})_\odot = 8.76 \pm 0.07$ and $Z_\odot = 0.0156$ from Caffau et al. (2008, 2009) to be consistent with the solar abundance values adopted in our SSP models (see Section 4).

(v) We use the cluster velocities to infer the dynamical mass of NGC 4449. We estimate the mass of NGC 4449 inside 2.88 kpc to be $M(<2.88 \text{ kpc}) = 3.15^{+3.16}_{-0.75} \times 10^9 M_{\odot}$; the upper mass limit within 30 arcmin is $\sim 3.6^{+3.6}_{-0.9} \times 10^{10} M_{\odot}$, significantly lower than the mass derived in the literature from H I data.

ACKNOWLEDGEMENTS

This work was based on LBT/MODS data. The LBT is an international collaboration among institutions in the United States, Italy, and Germany. LBT Corporation partners are the University of Arizona on behalf of the Arizona Board of Regents; Istituto Nazionale di Astrofisica, Italy; LBT Beteiligungsgesellschaft, Germany, representing the Max Planck Society, the Leibniz Institute for Astrophysics Potsdam, and Heidelberg University; the Ohio State University, and the Research Corporation, on behalf of the University of Notre Dame, University of Minnesota, and University of Virginia. We acknowledge the support from the LBT-Italian Coordination Facility for the execution of observations, data distribution, and reduction. FA and MT acknowledge funding from INAF PRIN-SKA-2017 programme 1.05.01.88.04. We thank the anonymous referee for his/her very nice report.

REFERENCES

- Adamo A., Östlin G., Zackrisson E., Papaderos P., Bergvall N., Rich R. M., Micheva G., 2011a, *MNRAS*, 415, 2388
- Adamo A., Östlin G., Zackrisson E., 2011b, *MNRAS*, 417, 1904
- Adamo A., Kruijssen J. M. D., Bastian N., Silva-Villa E., Ryon J., 2015, *MNRAS*, 452, 246
- Annibali F., Bressan A., Rampazzo R., Zeilinger W. W., Danese L., 2007, *A&A*, 463, 455
- Annibali F., Aloisi A., Mack J., Tosi M., van der Marel R. P., Angeretti L., Leitherer C., Sirianni M., 2008, *AJ*, 135, 1900
- Annibali F., Tosi M., Monelli M., Sirianni M., Montegriffo P., Aloisi A., Greggio L., 2009, *AJ*, 138, 169
- Annibali F., Grützbauch R., Rampazzo R., Bressan A., Zeilinger W. W., 2011a, *A&A*, 528, A19
- Annibali F., Tosi M., Aloisi A., van der Marel R. P., 2011b, *AJ*, 142, 129 (A11)
- Annibali F., Tosi M., Aloisi A., van der Marel R. P., Martinez-Delgado D., 2012, *ApJ*, 745, L1
- Annibali F. et al., 2013, *AJ*, 146, 144
- Annibali F. et al., 2017, *ApJ*, 843, 20
- Bajaja E., Huchtmeier W. K., Klein U., 1994, *A&A*, 285, 385
- Bastian N., Lardo C., 2017, *Annu. Rev. Astron. Astrophys.*, reprint ([arXiv:1712.01286](https://arxiv.org/abs/1712.01286))
- Berg D. A. et al., 2012, *ApJ*, 754, 98
- Bertelli G., Mateo M., Chiosi C., Bressan A., 1992, *ApJ*, 388, 400
- Billett O. H., Hunter D. A., Elmegreen B. G., 2002, *AJ*, 123, 1454
- Bond H. E., 2015, *AJ*, 149, 132
- Bouwens R. J. et al., 2012, *ApJ*, 752, L5
- Bressan A., Chiosi C., Fagotto F., 1994, *ApJS*, 94, 63
- Caffau E., Ludwig H.-G., Steffen M., Ayres T. R., Bonifacio P., Cayrel R., Freytag B., Plez B., 2008, *A&A*, 488, 1031
- Caffau E., Maiorca E., Bonifacio P., Faraggiana R., Steffen M., Ludwig H.-G., Kamp I., Busso M., 2009, *A&A*, 498, 877
- Carretta E., Bragaglia A., Gratton R. G., Leone F., Recio-Blanco A., Lucatello S., 2006, *A&A*, 450, 523
- Cenarro A. J., Cardiel N., Gorgas J., Peletier R. F., Vazdekis A., Prada F., 2001, *MNRAS*, 326, 959
- Cenarro A. J., Gorgas J., Cardiel N., Vazdekis A., Peletier R. F., 2002, *MNRAS*, 329, 863
- Cenarro A. J., Cardiel N., Vazdekis A., Gorgas J., 2009, *MNRAS*, 396, 1895
- Cignoni M. et al., 2016, *ApJ*, 833, 154
- Concas A., Pozzetti L., Moresco M., Cimatti A., 2017, *MNRAS*, 468, 1747
- Conselice C. J., 2006, *ApJ*, 639, 120
- Cook D. O. et al., 2012, *ApJ*, 751, 100
- Dalcanton J. J. et al., 2009, *ApJS*, 183, 67
- D'Antona F., Vesperini E., D'Ercole A., Ventura P., Milone A. P., Marino A. F., Tailo M., 2016, *MNRAS*, 458, 2122
- Dolphin A., 1997, *New Astron.*, 2, 397
- Fagotto F., Bressan A., Bertelli G., Chiosi C., 1994a, *A&AS*, 104, 365
- Fagotto F., Bressan A., Bertelli G., Chiosi C., 1994b, *A&AS*, 105, 29
- Filippenko A. V., 1982, *PASP*, 94, 715
- Flores-Durán S. N., Peña M., Ruiz M. T., 2017, *A&A*, 601, A147
- Gallart C., Aparicio A., Bertelli G., Chiosi C., 1996, *AJ*, 112, 1950
- García-Rojas J., Peña M., Flores-Durán S., Hernández-Martínez L., 2016, *A&A*, 586, A59
- Gillett F. C., Jacoby G. H., Joyce R. R., Cohen J. G., Neugebauer G., Soifer B. T., Nakajima T., Matthews K., 1989, *ApJ*, 338, 862
- Goddard Q. E., Bastian N., Kennicutt R. C., 2010, *MNRAS*, 405, 857
- González J. J., 1993, PhD thesis, Washington Univ., Seattle, WA
- Gratton R. G., Carretta E., Bragaglia A., 2012, *A&AR*, 20, 50
- Greggio L., Renzini A., 1983, *Mem. Soc. Astron. Ital.*, 54, 311
- Grevesse N., Sauval A. J., 1998, *Space Sci. Rev.*, 85, 161
- Grocholski A. J., van der Marel R. P., Aloisi A., Annibali F., Greggio L., Tosi M., 2012, *AJ*, 143, 117
- Guseva N. G., Izotov Y. I., Stasińska G., Fricke K. J., Henkel C., Papaderos P., 2011, *A&A*, 529, A149
- Hanuschik R. W., 2003, *A&A*, 407, 1157
- Hasselquist S. et al., 2017, *ApJ*, 845, 162
- Haurberg N. C., Rosenberg J., Salzer J. J., 2013, *ApJ*, 765, 66
- Hill V., François P., Spite M., Primas F., Spite F., 2000, *A&A*, 364, L19
- Hunter D. A., 2001, *ApJ*, 559, 225
- Hunter D. A., Wilcots E. M., van Woerden H., Gallagher J. S., Kohle S., 1998, *ApJ*, 495, L47
- Hunter D. A., O'Connell R. W., Gallagher J. S., Smecker-Hane T. A., 2000, *AJ*, 120, 2383
- Hunter D. A., Rubin V. C., Swaters R. A., Sparke L. S., Levine S. E., 2002, *ApJ*, 580, 194
- Hunter D. A., Rubin V. C., Swaters R. A., Sparke L. S., Levine S. E., 2005, *ApJ*, 634, 281
- Hwang N., Park H. S., Lee M. G., Lim S., Hodge P. W., Kim S. C., Miller B., Weisz D., 2014, *ApJ*, 783, 49
- Izotov Y. I., Thuan T. X., 1999, *ApJ*, 511, 639
- Jacoby G. H., Morse J. A., Fullton L. K., Kwitter K. B., Henry R. B. C., 1997, *AJ*, 114, 2611
- Jacoby G. H., Ciardullo R., De Marco O., Lee M. G., Herrmann K. A., Hwang H. S., Kaplan E., Davies J. E., 2013, *ApJ*, 769, 10
- Jacoby G. H., De Marco O., Davies J., Lotarevich I., Bond H. E., Harrington J. P., Lanz T., 2017, *ApJ*, 836, 93
- Johnson J. A., Ivans I. I., Stetson P. B., 2006, *ApJ*, 640, 801
- Karczewski O. Ł. et al., 2013, *MNRAS*, 431, 2493
- Kaufer A., Venn K. A., Tolstoy E., Pinte C., Kudritzki R.-P., 2004, *AJ*, 127, 2723
- Kauffmann G., White S. D. M., 1993, *MNRAS*, 261, 921
- Kirby E. N., Cohen J. G., Smith G. H., Majewski S. R., Sohn S. T., Guhathakurta P., 2011, *ApJ*, 727, 79
- Kniazhev A. Y., Grebel E. K., Pustilnik S. A., Pramskij A. G., Zucker D. B., 2005, *AJ*, 130, 1558
- Korn A. J., Maraston C., Thomas D., 2005, *A&A*, 438, 685
- Kumari N., James B. L., Irwin M. J., 2017, *MNRAS*, 470, 4618
- Lanfranchi G. A., Matteucci F., 2003, *MNRAS*, 345, 71
- Larsen S. S., 2008, *A&A*, 477, L17
- Larsen S. S., Richtler T., 2000, *A&A*, 354, 836
- Leaman R., Cole A. A., Venn K. A., Tolstoy E., Irwin M. J., Szeifert T., Skillman E. D., McConnachie A. W., 2009, *ApJ*, 699, 1
- Leaman R. et al., 2013, *ApJ*, 767, 131
- Lemasle B. et al., 2014, *A&A*, 572, A88
- Lilly S. J., Tresse L., Hammer F., Crampton D., Le Fevre O., 1995, *ApJ*, 455, 108
- McQuinn K. B. W. et al., 2010a, *ApJ*, 721, 297

- McQuinn K. B. W. et al., 2010b, *ApJ*, 724, 49
- Magrini L., Leisy P., Corradi R. L. M., Perinotto M., Mampaso A., Vílchez J. M., 2005, *A&A*, 443, 115
- Marconi G., Matteucci F., Tosi M., 1994, *MNRAS*, 270, 35
- Martin C. L., 1998, *ApJ*, 506, 222
- Martínez-Delgado D. et al., 2012, *ApJ*, 748, L24
- Martocchia S. et al., 2017, *MNRAS*, 468, 3150
- Matteucci F., Recchi S., 2001, *ApJ*, 558, 351
- Matteucci F., Tosi M., 1985, *MNRAS*, 217, 391
- Minniti D., Rejkuba M., 2002, *ApJ*, 575, L59
- Monelli M. et al., 2010, *ApJ*, 722, 1864
- Mucciarelli A., Origlia L., Ferraro F. R., 2010, *ApJ*, 717, 277
- Navarro J. F., Frenk C. S., White S. D. M., 1997, *ApJ*, 490, 493
- Norris J. E., Yong D., Venn K. A., Gilmore G., Casagrande L., Dotter A., 2017, *ApJS*, 230, 28
- Origlia L., Rich R. M., Castro S., 2002, *AJ*, 123, 1559
- Osterbrock D. E., 1989, *Astrophysics of Gaseous Nebulae and Active Galactic Nuclei*. University Science Books, Mill Valley, CA
- Pancino E. et al., 2017, *A&A*, 601, A112
- Pease F. G., 1928, *PASP*, 40, 342
- Pellerin A., Meyer M. M., Calzetti D., Harris J., 2012, *AJ*, 144, 182
- Peña M., Stasińska G., Richer M. G., 2007, *A&A*, 476, 745
- Pilyugin L. S., Grebel E. K., Zinchenko I. A., 2015, *MNRAS*, 450, 3254
- Piotto G. et al., 2015, *AJ*, 149, 91
- Puzia T. H., Sharina M. E., 2008, *ApJ*, 674, 909
- Puzia T. H., Kissler-Patig M., Brodie J. P., Schroder L. L., 2000, *AJ*, 120, 777
- Puzia T. H., Saglia R. P., Kissler-Patig M., Maraston C., Greggio L., Renzini A., Ortolani S., 2002, *A&A*, 395, 45
- Puzia T. H., Perrett K. M., Bridges T. J., 2005, *A&A*, 434, 909
- Rampazzo R., Annibali F., Bressan A., Longhetti M., Padoan F., Zeilinger W. W., 2005, *A&A*, 433, 497
- Renzini A. et al., 2015, *MNRAS*, 454, 4197
- Rich R. M., Collins M. L. M., Black C. M., Longstaff F. A., Koch A., Benson A., Reitzel D. B., 2012, *Nature*, 482, 192
- Sacchi E. et al., 2016, *ApJ*, 830, 3
- Sacchi E. et al., 2018, *ApJ*, submitted
- Serven J., Worthey G., 2010, *AJ*, 140, 152
- Sharina M. E., Puzia T. H., Krylatyh A. S., 2007, *Astrophys. Bull.*, 62, 209
- Sharina M. E., Chandar R., Puzia T. H., Goudfrooij P., Davoust E., 2010, *MNRAS*, 405, 839
- Shetrone M. D., Bolte M., Stetson P. B., 1998, *AJ*, 115, 1888
- Shetrone M. D., Côté P., Sargent W. L. W., 2001, *ApJ*, 548, 592
- Skillman E. D. et al., 2017, *ApJ*, 837, 102
- Smith J. D. T. et al., 2007, *PASP*, 119, 1133
- Storey P. J., Hummer D. G., 1995, *MNRAS*, 272, 41
- Strader J., Brodie J. P., Huchra J. P., 2003, *MNRAS*, 339, 707
- Strader J., Brodie J. P., Cenarro A. J., Beasley M. A., Forbes D. A., 2005, *AJ*, 130, 1315
- Strader J., Seth A. C., Caldwell N., 2012, *AJ*, 143, 52
- Thomas D., Maraston C., Bender R., 2003, *MNRAS*, 339, 897
- Tolstoy E., Venn K. A., Shetrone M., Primas F., Hill V., Kaufer A., Szeifert T., 2003, *AJ*, 125, 707
- Tolstoy E., Hill V., Tosi M., 2009, *ARA&A*, 47, 371
- Tornambe A., Matteucci F., 1986, *MNRAS*, 223, 69
- Tosi M., Greggio L., Marconi G., Focardi P., 1991, *AJ*, 102, 951
- Trager S. C., Worthey G., Faber S. M., Burstein D., González J. J., 1998, *ApJS*, 116, 1
- Tripicco M. J., Bell R. A., 1995, *AJ*, 110, 3035
- Valdez-Gutiérrez M., Rosado M., Puerari I., Georgiev L., Borissova J., Ambrocio-Cruz P., 2002, *AJ*, 124, 3157
- van der Marel R. P., Kallivayalil N., 2014, *ApJ*, 781, 121
- van Zee L., Haynes M. P., 2006, *ApJ*, 636, 214
- Vazdekis A., Cenarro A. J., Gorgas J., Cardiel N., Peletier R. F., 2003, *MNRAS*, 340, 1317
- Venn K. A. et al., 2001, *ApJ*, 547, 765
- Venn K. A., Tolstoy E., Kaufer A., Skillman E. D., Clarkson S. M., Smartt S. J., Lennon D. J., Kudritzki R. P., 2003, *AJ*, 126, 1326
- Watkins L. L., Evans N. W., An J. H., 2010, *MNRAS*, 406, 264
- Weidner C., Kroupa P., Pflamm-Altenburg J., Vazdekis A., 2013, *MNRAS*, 436, 3309
- Weisz D. R., Dolphin A. E., Skillman E. D., Holtzman J., Gilbert K. M., Dalcanton J. J., Williams B. F., 2014, *ApJ*, 789, 147
- Worthey G., Ottaviani D. L., 1997, *ApJS*, 111, 377
- Worthey G., Faber S. M., Gonzalez J. J., Burstein D., 1994, *ApJS*, 94, 687
- Yan Z., Jerabkova T., Kroupa P., 2017, *A&A*, 607, A126

APPENDIX: LICK AND CA II TRIPLET INDICES DERIVED FOR GCS IN NGC 4449

Table A1. Lick and CaII triplet indices derived for GCs in NGC 4449.

Name	CN ₁ eCN ₁	CN ₂ eCN ₂	Ca4227 eCa4227	G4300 eG4300	Fe4383 eFe4383	Ca4455 eCa4455	Fe4531 eFe4531	C ₂ 4668 eC ₂ 4668	H β eH β	Fe5015 eFe5015	Mg1 eMg1	Mg2 eMg2	Mgb eMgb	Fe5270 eFe5270	Fe5335 eFe5335	H γ A eH γ A	H γ F eH γ F	CaT* eCaT*
CL20	-0.10	-0.06	0.3	1.4	-0.5	0.4	0.0	-0.9	2.0	1.7	0.042	0.078	1.1	1.3	1.1	-0.2	0.6	7.0
CL20	0.01	0.02	0.2	0.5	0.7	0.3	0.5	0.9	0.3	0.7	0.009	0.009	0.3	0.4	0.4	0.5	0.3	0.8
CL67	-0.13	-0.07	0.0	-2.8	-1.1	-0.2	0.1	-6	6.4	0.0	0.04	0.08	0.7	0.4	0.1	10.1	7.3	7.0
CL67	0.02	0.03	0.4	0.9	1.3	0.6	1.0	2	0.6	2.0	0.02	0.02	0.8	0.9	1.0	0.7	0.4	3.0
CL76	-0.081	-0.07	0.34	3.1	0.2	1.0	2.6	-0.05	2.0	2.1	0.058	0.125	1.4	1.7	1.5	-1.6	0.1	6.5
CL76	0.005	0.01	0.08	0.2	0.2	0.2	0.1	0.34	0.1	0.3	0.006	0.004	0.1	0.1	0.1	0.2	0.1	0.3
CL72	0.02	0.07	0.8	3.4	1.4	0.0	2.0	-0.2	1.6	3.9	0.054	0.111	1.6	1.9	1.3	-1.7	0.4	6.9
CL72	0.01	0.02	0.2	0.4	0.5	0.3	0.4	0.6	0.2	0.6	0.008	0.007	0.2	0.3	0.3	0.4	0.2	0.6
CL75	-0.02	0.02	0.6	3.2	1.0	0.1	1.4	1.5	1.9	2.1	0.044	0.078	0.8	1.5	1.0	0.2	0.4	3.5
CL75	0.01	0.02	0.2	0.4	0.6	0.3	0.5	0.8	0.3	0.7	0.009	0.009	0.3	0.3	0.4	0.5	0.3	0.8
CL79	-0.076	-0.05	0.55	2.8	1.2	0.7	2.2	1.9	2.0	2.8	0.058	0.107	1.2	1.5	1.1	-1.2	0.8	6.4
CL79	0.005	0.01	0.08	0.2	0.2	0.2	0.2	0.3	0.1	0.4	0.006	0.004	0.1	0.1	0.1	0.2	0.1	0.3
CL58	-0.01	0.02	0.6	2.7	0.7	1.0	2.1	0.7	2.6	1.8	0.08	0.14	1.7	1.4	1.2	-0.6	0.8	7
CL58	0.02	0.02	0.3	0.6	0.9	0.4	0.7	1.0	0.5	1.0	0.01	0.01	0.5	0.5	0.6	0.7	0.4	1
CL52	-0.072	-0.04	0.5	2.9	0.9	1.1	1.9	0.5	2.2	3.4	0.066	0.118	1.2	1.5	1.2	-1.2	0.9	6.9
CL52	0.009	0.01	0.2	0.4	0.4	0.2	0.3	0.6	0.2	0.5	0.008	0.007	0.2	0.3	0.3	0.3	0.2	0.6
CL3	-0.077	-0.03	0.61	2.5	2.1	0.2	0.5	-0.7	1.9	3.2	0.070	0.112	1.9	1.2	1.4	-1.1	1.2	6.2
CL3	0.005	0.10	0.08	0.2	0.2	0.2	0.2	0.4	0.1	0.4	0.006	0.005	0.1	0.2	0.2	0.2	0.1	0.4
CL77	-0.098	-0.08	0.6	3.1	1.6	1.0	2.2	3.3	2.0	1.6	0.052	0.100	1.1	1.5	0.9	-2.4	0.7	6.1
CL77	0.007	0.10	1.0	0.3	0.3	0.2	0.2	0.4	0.1	0.4	0.007	0.005	0.2	0.2	0.2	0.3	0.1	0.4
CL27	-0.092	-0.07	0.7	2.0	2.2	0.8	2.0	1.8	1.9	2.9	0.069	0.117	1.5	1.7	1.3	-1.7	0.9	6.1
CL27	0.008	0.01	0.1	0.3	0.4	0.2	0.3	0.5	0.2	0.5	0.007	0.007	0.2	0.2	0.2	0.3	0.2	0.5
CL24	-0.11	-0.09	0.0	3.1	0.6	-0.2	2.4	4.7	1.3	3	0.09	0.13	1.5	0.8	0.8	-2.6	0.1	5
CL24	0.02	0.02	0.3	0.6	0.8	0.4	0.7	1.0	0.4	1	0.01	0.01	0.5	0.5	0.6	0.7	0.4	1

 This paper has been typeset from a \LaTeX file prepared by the author.